doi:10.26443/seismica.v5i2.1588

SEISMICA

Spatial Changes in Earthquake-Generated Ground Motion Observations: An Examination of Seven Small Aperture Arrays in Southern California

Debi Kilb *[1], **Frank Vernon** [1]

[1]Scripps Institution of Oceanography, University of California, San Diego, La Jolla, California, 92093-0225, USA

Author contributions: *Conceptualization*: F. Vernon. *Data Curation*: D. Kilb and F. Vernon. *Formal Analysis*: D. Kilb and F. Vernon. *Funding Acquisition*: F. Vernon. *Investigation*: D. Kilb and F. Vernon. *Methodology*: D. Kilb and F. Vernon. *Software*: D. Kilb. *Validation*: D. Kilb. *Visualization*: D. Kilb. *Writing – original draft*: D. Kilb. *Writing – review & editing*: D. Kilb and F. Vernon.

Abstract Ground motions recorded at one location are often extrapolated to nearby regions within a given radius. We explore the appropriateness of spatial extrapolation using data from seven small aperture (diameters < 3km) seismic networks in southern California that were operational for a year or more. Five of the seven arrays traverse the San Jacinto fault, and two locate off-fault. From our base catalog (4038 M2.5+ earthquakes; September 2010 - June 2023), we remove temporally overprinted waveforms from nearby events (≤ 5 km) in quick succession (≤ 5 minutes) and data with non-viable waveforms. These 200 samples per second data are filtered at 0.5-25 Hz and must have signal-to-noise ratios 2.5+. Peak ground acceleration and ground velocity are derived individually from the maximum absolute values of each of the three-component waveforms. We compare ground motion observations with empirical estimates from (Abrahamson et al., 2014). On average, arrays deployed across fault zones consistently record ground motions above empirical expectations, whereas off-fault arrays record ground motions at or slightly below empirical expectations. For all seven networks, the coefficient of variation shows large standard deviations at 26-38% of the mean, suggesting extrapolation should be done with caution even within small regions (< 3km).

Production Editor:
Yen Joe Tan
Handling Editor:
Pablo Heresi
Copy & Layout Editor:
Hannah F. Mark

Received:
February 11, 2025
Accepted:
July 1, 2026
Published:
August 28, 2026

Non-technical summary Commonly, if ground motions are not known at one location, the ground motions recorded at a nearby location are assumed to be representative of the extended region. Here, we test if this type of spatial extrapolation is valid using data (4038 M2.5+ earthquakes; September 2010 - June 2023) recorded by seven small aperture arrays with spatial footprint diameters of 3 km or less. Five of these networks traverse portions of the San Jacinto Fault Zone in southern California, and two of the networks are located off-fault. We refine these data by removing non-viable signals, including overprinting of waveforms from nearby earthquakes in quick succession (within 5 km and 5 minutes of each other). Ground motions within the assumed fault zones are larger than the empirical estimates, whereas ground motions outside of the assumed fault zones are as expected or smaller than the empirical estimates. Surprisingly, we find deviations from mean ground motions across each network are large at 26%-38% for each channel. This suggests spatial extrapolation of ground motions should be done with caution even within these very small spatial footprints (array diameters in km: 0.15, 0.18, 0.37, 0.46, 1.10, 1.10, 2.90).

1 Introduction

Ground motion data are essential for a range of geoscience topics, including but not limited to earthquake early warning (Allen and Stogaitis, 2022), seismic hazard estimates (Iervolino et al., 2022), and identification of earthquake source directivity features (Kurzon et al., 2014; Hirakawa et al., 2023). In regions with sparse station coverage, researchers typically use extrapolation techniques, assuming they can estimate ground motions within a certain radius of a station based on the recordings from that station (Cochran et al., 2022). There are various ways to extrapolate measurements from one location to nearby regions. One option is to assume that the ground motions will be similar when extended to a given radius from the station or, alternatively, apply a damping factor that reduces the amplitude by a factor that scales with distance (Tamhidi et al., 2023). These simplified extrapolations can be misguided in regions of variable geological features, complex fault geometry, or pore pressure variability (Graves et al., 2008).

Ground motions within 3D sedimentary basin structures can generate surface waves at the basin edge, creating reverberations and significantly increasing ground motions (Vidale and Helmberger, 1988). Theoretical simulations of ground motions within the Los Angeles basin found that the scale factors for ground motion amplification depend on basin depth. For regions near Los Angeles, California, where the basin depth extends to 9 km, an amplification factor as large as six can be produced (Olsen, 2000). These types of basin resonance are well known, and current work is

*Corresponding author: dkilb@ucsd.edu

exploring how amplification, or alternative attenuation, occurs within and around fault zones, which is the aim of this work.

How ground motions are elevated or diminished can be categorized by three terms: source, path, and site terms (Douglas and Edwards, 2016; Parker et al., 2020; Zhang et al., 2022; Nye et al., 2022; Chang et al., 2025). An example of a source term effect is when an earthquake source has a strong directivity, producing more seismic energy in one direction than another (Kilb et al., 2002; Kurzon et al., 2014; Hirakawa et al., 2023). Path terms, on the other hand, are generated along the path from the earthquake source to the station. If the seismic wave path traverses only hard rock materials, the path term is typically minimal and does not substantially increase or decrease ground motions. In contrast, the ground motion typically increases if the path traverses primarily unconsolidated material or variable material strengths (Yang and Zhu, 2010; Sahakian et al., 2018). Influences near the recording station create site terms. Examples of site terms are small basin resonances or wind-generated signals created by the movement of trees in response to high winds (Johnson et al., 2019).

In regions where recording stations are located only a few kilometers apart, source and path effects are expected to be nearly identical, so observed differences in ground motions primarily reflect site effects (Anderson and Hough, 1984; Steidl et al., 1996; Sahakian et al., 2018; Nye et al., 2022). The reason for this assumption is that the path terms will be almost identical because the azimuth variations between the station/source span a small azimuth range, and in turn the source terms will be similar as well. This is the case for the seven small aperture arrays that we study in this work. Here, we investigate how variable site terms can be within seven small aperture (<3 km diameters) arrays and assume for a single quake that the source and path terms are essentially identical.

Site terms often modeled using Vs30 scaling, where Vs30 is the time-averaged shear-wave velocity within the top 30 meters of material at a site (Borcherdt, 1994). High values of Vs30 suggest the site lacks a large sediment layer, and the site is assumed to have low amplification factors. In comparison, low Vs30 values indicate thick sediment layers and, in turn, high amplification factors. Of course, there are exceptions to these theories where ground motions are either much larger or smaller than expected (Minson et al., 2020).

When direct Vs30 measurements are unavailable, additional information can be used as a proxy. One approach is to estimate Vs30 from topographic slope proxies (Wald and Allen, 2007), which use quantitative metrics, typically derived from digital elevation models (DEMs; Iwahashi and Pike, 2007). These slope-based methods broadly assume that flatter topography corresponds to thick basin sediments, whereas steeper topography is associated with hard-rock regions with minimal sediment cover (Heath et al., 2020). However, assuming a simple linear relationship between Vs30 and topography can be misleading. This concern is particularly relevant for engineering applications, as simplified site terms do not account for near-surface soil conditions that can experience nonlinear and permanent deformations (Trifunac, 2016). Alternatively, the terrain proxy assigns general class labels such as flat, hilly, or mountainous to specific regions (Yong et al., 2012; Yong, 2016) and the geology proxies uses mapped age and type of surface materials such as granite, alluvium, volcanic rock, or marine sediment (Wills et al., 2015). Each method has advantages and limitations. Many studies show that collectively integrating multiple data sources (e.g., DEM, slope, terrain class, and geology) produces more accurate Vs30 maps. These are termed Vs30 patchwork mosaics that enhance both spatial coverage and site-condition accuracy (Allen and Wald, 2007; Thompson et al., 2014; Parker et al., 2017; Heath et al., 2020; Huddleston et al., 2021; Li et al., 2022; Petersen et al., 2024).

Increasing the number of seismic stations in a region reduces the inter-station spacing lengths and allows for an increased understanding of ground motion variability. EarthScope's USArray deployment aimed to have station spacings of 70 km (IRIS Transportable Array, 2003), and the ShakeAlert earthquake early warning system deployed within western USA (California, Washington, and Oregon) strives to have ~10 km inter-station spacing (Given et al., 2014; Kohler et al., 2020; Lux et al., 2024). Small aperture arrays, a network of stations deployed 10's of meters apart, can explore nuances in ground motion variability within even smaller spatial footprints (e.g., Vernon et al., 1991; Ben-Zion et al., 2015; Share et al., 2017; Qiu et al., 2017; Zigone et al., 2019; Anthony et al., 2020; Qiu et al., 2021; Share et al., 2023, 2018).

Here, we explore data from seven small aperture arrays with spatial footprint diameters of 3 km or less. The aim is to understand better when ground motions recorded at one location can be reliably extrapolated to nearby regions and when they cannot. This work allows us to assess how variable ground motions can be within a well-defined small area sufficiently instrumented within and outside fault zones.

2 Seismic Networks and Data Selection

The seven small aperture network arrays were selected because they have 3-component data and were active for at least one year (Figures 1-2; Table S1). Array names use two-letter codes that represent the geographic region: BB = Blackburn Saddle, DW = Dry Wash, JF = Jackass Flat, PY = Pinyon Flat, RA = Ramona, SG = Sagebrush Flat, and TR = Transect. Two of these seven networks (PY and TR) are located away from the primary fault system, and five span the San Jacinto fault (BB, DW, JF, RA, and SG). All arrays are linear except for the PY array, which is two-dimensional (Table S2; Appendix A, Figures A1-A7).

We start with a base catalog of reviewed earthquakes spanning ~13 years, 2010-09-20 through 2023-06-30 (Kilb and Vernon, 2025a), including 4038 local magnitude (M_L) 2.5+ events. From this base catalog, we create subcatalogs limited to events within 150 km of the network centroid for each of the seven networks. Because of the spatial differences in the network centroids, these sub-catalogs differ from network to network (see Table S1; Figures 1-2), but this is not a concern because the catalogs are vast (each contains over ~11,000 waveforms that have passed the data quality restrictions) and can adequately provide general ground motion trends.

3 Data Preprocessing & Method

Data from the seven networks (Figure 3) are processed similarly, and the seismic data pre-processing includes four steps (Kilb and Vernon, 2025b). First, to eliminate waveform overprinting, which could result in misleading elevated ground motion measurements, we remove all earthquake pairs in the base catalog that are spatially (≤5 km) and temporally (≤5 minutes) close. We purposely process data in the base catalog, not the individual catalogs, to avoid introducing errors at the edges of the sub-catalog spatial boundaries. Using the entire base catalog is also time efficient as this processing is applied only once to the base catalog (i.e., not individually for each of the seven sub-catalogs). The overprinting removal process iteratively repeats until no additional data are flagged for removal, indicating all remaining data are more than 5 km and 5 minutes apart. This overprinting removal requirement is essential to ensure our derived ground motion values are measuring ground motions produced by a single earthquake, not multiple quakes. Overall, this process primarily flags events during the Salton Sea swarms in 2012, 2016, 2020, and 2021 (Kilb et al., 2021). Because our catalog includes only M_L 2.5+ events, some smaller event overprinting likely remains within these data. But, for cases when additional smaller events exist within the wavetrain, these smaller events are unlikely to substantially bias the results.

The data overprinting vetting is relatively harsh, removing 16% of the base catalog (649 of 4038 removed; 3389 retained; see Table S1). The overprinting test removed five of the six M5+ events. The event not removed was an M5.41 (ID ci15200401) from the Salton Sea region on 26 August 2012, which, according to our M_L 2.5+ catalog, was followed 7 minutes later by a nearby M_L 3.18 event. Although not flagged by the overprinting method because the 7-minute differential exceeded the 5-minute threshold, out of an abundance of caution, we remove this M_L 5.41 mainshock from consideration for two reasons. First, this event was the second of two M_L 5+ events during the 2012 Salton Sea swarm, which occurred ~1.5 hours after an earlier M_L 5.32 event (ID ci15199681) in the same region and thus occurred within a time frame of active aftershocks. Second, this event is the largest in our catalog, and undoubtedly, its large waveforms obscured many of the smaller earthquakes within the first 5 mins of the sequence (e.g., Kilb et al., 2007).

The second step in the data pre-processing applies an instrument response correction, removing the mean from the data traces and band-pass filtering for each waveform remaining after the overprinting tests. For these 200 samples per second data, we apply 4th-order bandpass Butterworth filters of 0.5 - 25 Hz. The low-pass level avoids low-frequency artifacts, and the high-pass avoids spurious high-frequency signals. The seismic waveform data is obtained through the IrisFetch Matlab interface (see Data and Code Availability section). In some cases, the returned data contains multiple data segments. When this occurs, we remove the mean from each sub-trace before combining the sub-traces into a final trace. This processing is essential, especially for the older data, because the DC offset can differ from sub-trace to sub-trace.

In the third data pre-processing step, we select robust waveforms requiring a signal-to-noise ratio (SNR) of 2.5 or above (see supplemental Figure S1). To measure SNR, we rely on theoretical P-wave (V_p; 6.5 km/s) and S-wave (V_s; 2 km/s) speeds and estimate theoretical P- and S-wave arrival times at each station using linear relationships:

$$P_{arrival} = Disthypo/V_p \tag{1}$$

$$S_{arrival} = Disthypo/V_s \tag{2}$$

$P_{arrival}$ and $S_{arrrival}$ are the theoretical P-wave and S-wave arrival times, respectively. $Disthypo$ is the hypocentral distance in kilometers between the earthquake and the station, calculated using the GRS80 reference ellipsoid. These simplistic linear estimates are not exact as they do not account for the earth's curvature or velocity depth differences. However, these estimates are appropriate for our purposes as the aim is simply to select the data of interest, a noise window, and estimate a SNR, so exact values are not required.

The noise waveform snippet is ten seconds long, extending from 12 seconds before $P_{arrival}$ through 2 seconds before $P_{arrival}$. This two-second gap between the end of the noise trace and the expected P-wave arrival is precautionary and allows for errors in the theoretical seismic wave arrival time estimates. The data window encompasses data from two seconds before $P_{arrival}$ through 30 seconds after $S_{arrival}$. In this way, the duration of each data window is variable, resulting in longer durations for more distant events when the P- and S-wave separation times are larger (see supplemental Figure S2). We calculate SNRs by dividing the maximum absolute amplitude of the data snippet by the maximum absolute amplitude of the noise snippet (Kilb and Vernon, 2025b).

The SNR criterion removes most of the bad data, but additional non-viable signals, those unrelated to a single earthquake, may still be retained. Given this, a fourth data quality test is implemented to vet how the observed ground motion amplitudes statistically differ from empirically expected values. Empirical estimates are derived using the Abrahamson et al. (2014) NGA-West2 ground-motion model, which provides predictions of horizontal peak ground acceleration (PGA) and peak ground velocity (PGV) for shallow crustal earthquakes in active crustal regions such as California. All empirical estimates are computed assuming a reference rock site condition (Vs30 ≈ 760 m/s), rather than using variable site-specific Vs30 values. Although this model

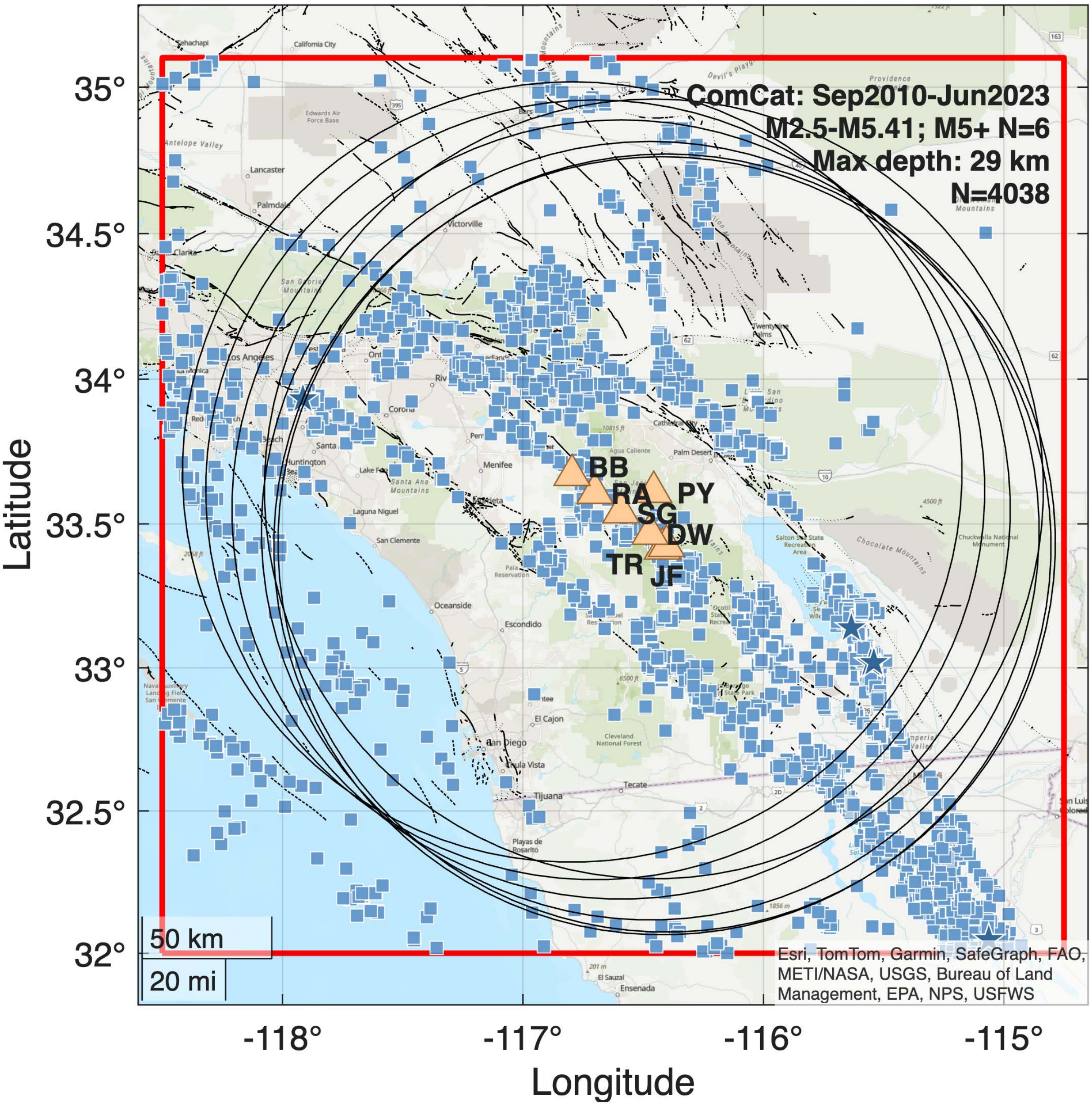

Figure 1 Study region in southern California. A base catalog of 4038 events (red square region; M_L 2.5+; 2010-09-20 through 2023-06-30; latitudes 32.0 to 35.1; longitudes -118.5 to -114.75; Kilb and Vernon, 2025a) is used to identify and remove overprinted events (events within 5 km and 5 mins) that have the potential to elevate ground motions misleadingly. Earthquake locations of M_L<5 and M_L5+ are depicted with the blue squares and stars, respectively. Labeled orange triangles are the seven network centroids and network codes. The final data of interest are sub-catalogs that contain events within 150 km of each network centroid (circular regions), events outside of these circles, but inside the red box were only used in the overprinting evaluation (Kilb and Vernon, 2025a).

was formulated for horizontal components only, we extend its use to vertical motions in this study to provide a more complete representation of the ground-motion field. The observed PGA and PGV are derived from the acceleration (HN* channels) and velocity (HH* channels) data, respectively (Kilb and Vernon, 2025b). PGA primarily captures high-frequency motion, whereas PGV is more sensitive to intermediate frequencies, making both robust measures of ground-motion intensity used in seismic hazard studies (Wald et al., 1999).

Quantitative measurements are made using the ratio of the empirically predicted ground motions to the observed values. Ratios below (above) zero indicate the observed ground motions were greater than (less than) expected. These ratios are evaluated using Matlab's *isoutlier* routine, using the 'mean' method that flags elements that are three or more standard deviations from the mean.

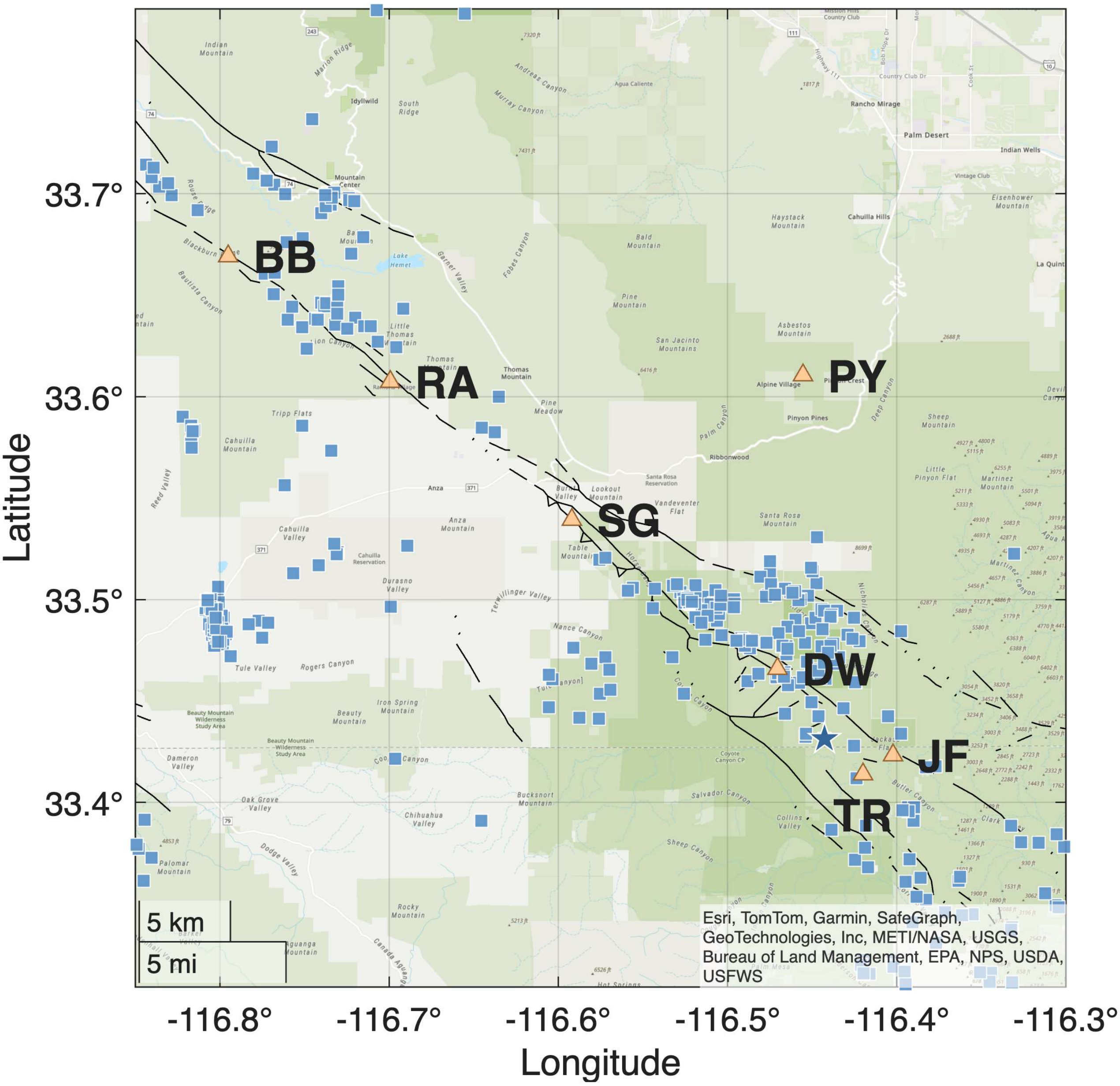

Figure 2 Network location map showing the spatial extent of the seven network centroids (orange triangles; BB, RA, SG, PY, DW, JF, and TR). Five networks are within the San Jacinto fault zone (BB, RA, SG, DW, and JF), and two are not (PY and TR). Earthquake locations of M_L<5 and M_L5+ are depicted with the blue squares and stars, respectively.

4 Results

4.1 Network-Wide SNR Distributions

The SNR restriction (SNR 2.5+) retains a high percentage of the data, ranging from 94.1% for the SG network to above 99% for the BB, DW, and PY networks (see supplemental Figure S3). These high percentages suggest that these data are of high quality. Although not shown here, we found that examining the SNR as a function of time can confirm times of instrumentation issues. Specifically, a step change in the SNR temporal behavior indicates an instrumentation change. We did not use the temporal evolution of SNR to identify problematic stations, but we did use it to confirm that instrumentation issues were at play when examining suspect data.

The SNR histograms from the seven arrays have different distributions (see supplemental Figure S3). Histograms from networks SG, RA, and PY have a similar distribution, showing a general tapering trend, with substantially more smaller SNR measurements than larger ones. Differing from that, histogram distributions for the other four networks (TR, JF, BB, and DW) are more rectangular. These differences stem from the fact that the SG, RA, and PY arrays recorded fewer events at close distances than the other four arrays. The larger number of small event-station distances for the other four arrays results in an elevated number of

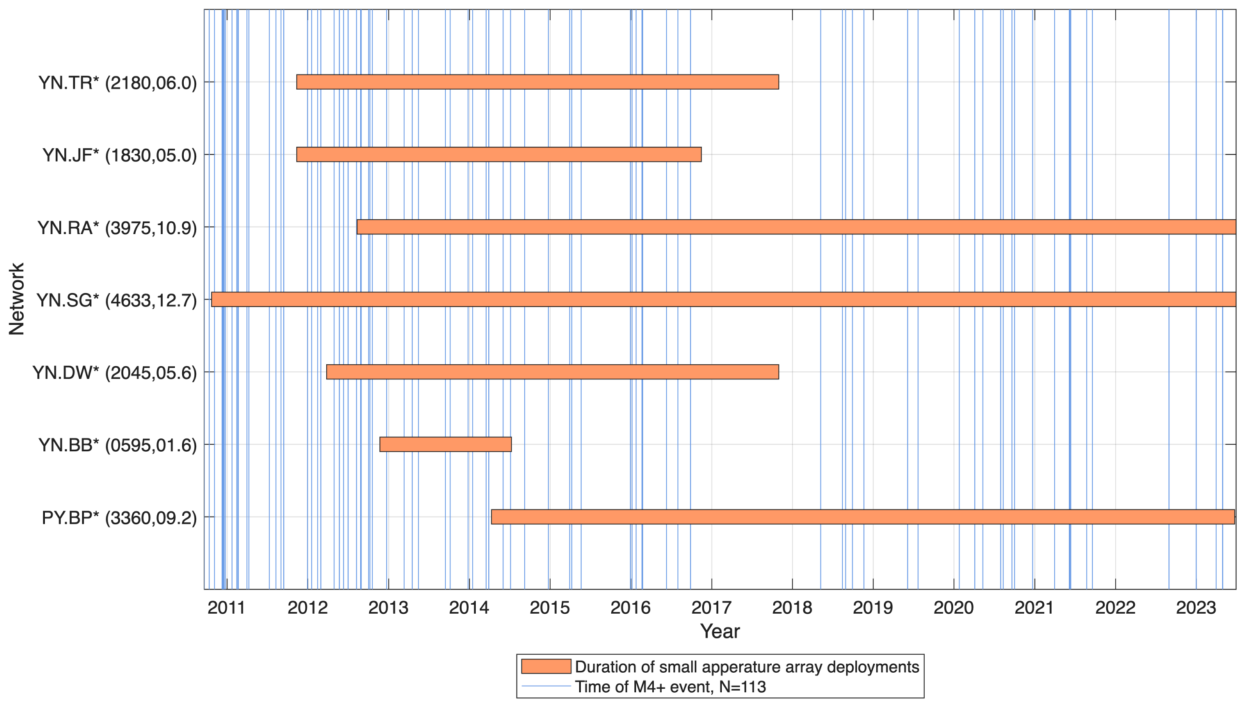

Figure 3 Deployment durations for this study's seven small aperture arrays (temporal durations indicated by orange bar lengths; numbers in parenthesis are duration days and years, respectively). All networks have a deployment span of a year or more. Although some networks are still running, in this study, we limit the collective temporal extent of data to 20 September 2010 through 30 June 2023. Blue vertical lines indicate times of M4+ earthquakes within the study region. Interestingly, in 2017, there were no M4+ earthquakes.

higher SNR ratios and, in turn, the rectangular-shaped histogram distribution.

4.2 Station-Level Variability in SNR within each Network

Next, we investigate the variability of the SNR distributions between individual stations within each network. For arrays BB, DW, JF, and PY, the SNR distributions are similar for all stations within the network, as expected for such small-footprint networks. Three arrays (RA, TR, and SG), however, show significant differences in the SNR distributions. The SNR distribution differences for the SG stations are the most pronounced, showing spikes in low SNR values at stations SGBFA, SGBN1, and SGBS3 (see Supplementary Figure S4), which stem from instrumental problems. These issues arose for stations SGBFA and SGBN1 in late 2011 and early 2012 and were subsequently corrected. The SGBS3 issues are less problematic, beginning in ~2021. For the RA and TR networks, stations RA09 and TR01 have a much larger number of flagged SNR measurements (i.e., SNR < 2.5) than the other RA and TR station reports, respectively (see Supplementary Figures S5-S6). The low SNR values at RA09 are caused by a relatively short-lived instrumental issue at the end of 2015, extending through a portion of 2016. Similarly, the low SNR values at TR01 were also caused by instrumental issues, primarily during portions of 2015 and portions of 2017. In all cases, the SNR threshold tests successfully flagged these bad data, which we removed from the catalog.

Implementing our non-viable waveform tests flags less than 1% of these data (1020 waveforms out of 213,163 that passed the overprinting and SNR tests). We qualitatively examine each flagged waveform and associated spectral signal (see supplementary S7). This vetting process identified and removed 350 nonviable waveforms (350 out of 1020 or 34%; Table S3; Kilb and Vernon, 2025c, see Data and Code availability section). Regardless of the network, we find no dependency between discarded waveforms and depth or magnitude. These discarded signals contain clipped data, low-frequency energy contamination, or SNR just above the 2.5 thresholds (i.e., ~2.5-5). The BB network data was the only array that did not flag waveforms for removal. This likely resulted because this array was deployed for the shortest duration (see Figure 3) and was not operational during most of the robust Salton Sea swarms.

4.3 Characteristics of Discarded Waveforms

Most of the non-viable waveforms were from the RA network. There were 234 RA waveforms discarded, whereas only 41 or less were discarded for the other six arrays (see Table S3). In all cases, the discarded RA waveforms were reporting higher than expected amplitudes. The primary reason for the large amount of corrupt RA waveform data is twofold. First, most of these waveforms are from smaller events at epicentral distances of ~85 km or more, and therefore the maximum amplitudes generated by these earthquakes are relatively small (acceleration <0.14 g). For the RA network configuration, these small amplitudes can be overprinted by larger signals generated by cars and trucks from the nearby roadway (See Supplementary Figure S8). This is particularly true for stations near the roadway: RA08 had 93 discarded waveforms, and RA07 and RA09 both had 47 discarded waveforms. Collectively, discarded waveforms from these three stations made up 80% of the non-viable RA data. Secondly, many of the RA discarded events occurred during prolific Salton Sea swarms, in particular, the swarms in 2012, 2020, and 2021. Elevated ground motions during these swarms are not a surprise, as these swarms contained many events below M2.5, which were not accounted for in our overprinted removal processing.

4.4 Observed vs. Empirical Ground Motions

Although the arrays are spatially compact, small variations in source-to-site distance, radiation pattern, and site conditions can still dominate absolute peak amplitudes. Comparing observations to empirical estimates provides a reference frame for identifying residual ground-motion behavior that is spatially coherent across each array. To that aim, we next evaluate the distribution of peak ground motions across each array compared to empirical estimates (Abrahamson et al., 2014). The first thing we investigate is if there are any obvious differences between ground motions recorded at arrays that traverse faults (BB, DW, JF, SG, and RA) in comparison with ground motions recorded by arrays deployed in regions that lack a well-developed fault system (TR and PY). We find that arrays deployed within the fault zone tend to record larger PGV and PGA than expected, and arrays not deployed within the fault zone (TR and PY) show PGV and PGA values as expected or slightly smaller than expected (Figure 4). Specifically, networks BB, JF, and SG observe ground motions larger than expected, as do RA and DW, but to a lesser extent. Data from TR report values closest to the empirical results. Notably, PY is the only network that records ground motions smaller than empirically expected.

4.5 Intra-Array Variability in Maximum Ground Motions

Using our refined data, individually for each earthquake and each channel within an array, we compute the mean and standard deviations of the PGV and PGA values. We calculate the coefficient of variance (COV) from these values, namely, the standard deviation divided by the mean. The COV measures how variable the findings are across the array, where large percentages indicate greater variability than smaller percentages. For proper comparison, we limit these values to only those from earthquakes recorded by all stations and all three channels within a network. We find the coefficients of variance range from 26% to 38%, with an assumed minimum uncertainty of 4% (Figure 5). The largest variabil-

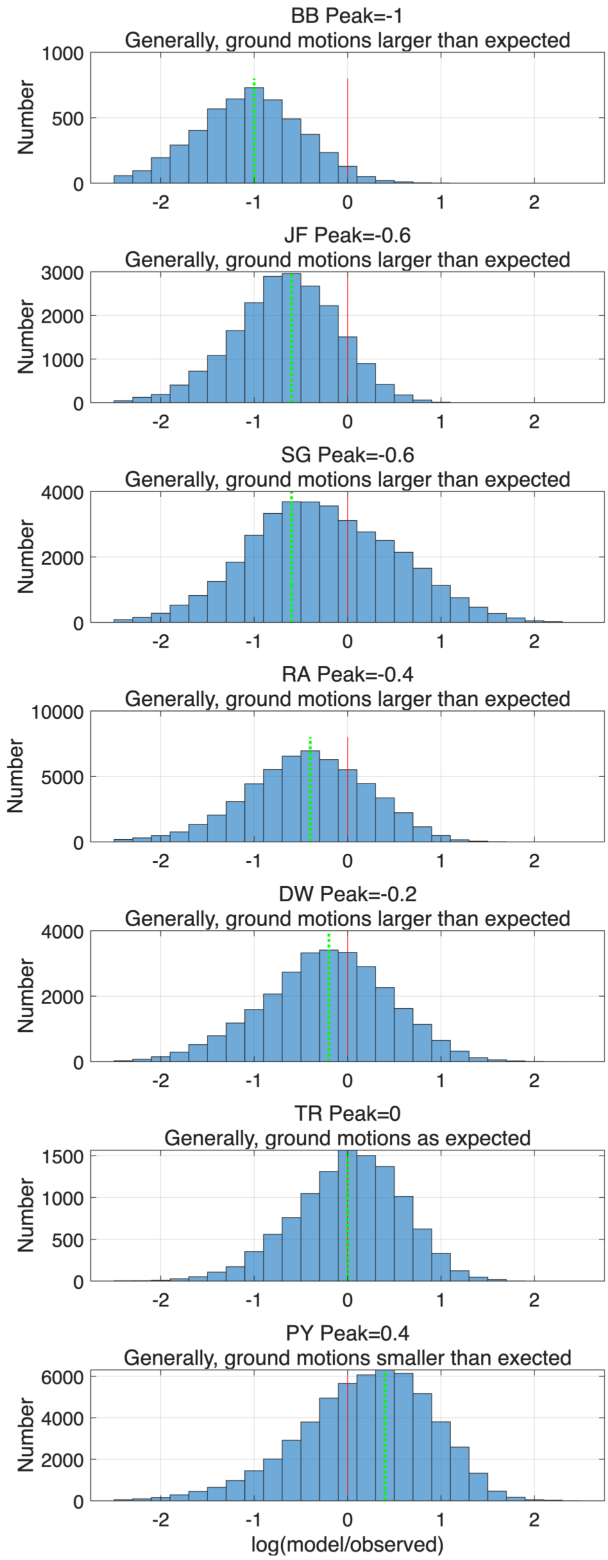

Figure 4 Summary of overall results, including the expected empirical model results (red line) and observed mean results (green dashed line). Histograms of log(model/observed) ground motions for each network ordered from smaller than expected motions (top; BB array) to larger than expected motions (bottom; PY array). Notice that the two bottom histograms show the least deviation from the expected value (dashed vertical green line close to the vertical red line), and both these arrays are off-fault. The top five histograms are from arrays within the fault zone and show more deviation than the off-fault arrays.

ity is found within the SG array at 38%, which is confirmed by the much wider histogram distribution in the SG data in Figure 4. The SG array is the shortest of all the arrays at 0.15 km in length. Therefore, the stations are closer together than in other networks, which suggests its COV might be smaller than the others, but that is not what we observe. We posit that this large variability stems from the multiple basin structures within this region that produce signal reverberations that can potentially increase ground motion variability.

4.6 Earthquakes that generate Maximum Ground Motions

Next, we track the largest ground motions recorded by each station (Table S4a-b; Kilb and Vernon, 2025d). The data considered include only events recorded by all network stations on all three channels. Within the DW network, stations DW11 and DW12 were installed ~2.5 years after the other stations (DW01-DW10), which reduced the potential DW data range to start when DW11 and DW12 were first installed on 2014-10-17. Because of these networks' small spatial footprints, the expectation is that stations within a given array would report the same earthquake as producing the largest ground motions across the entire array. That is not what we found. The percentage of stations that select the same event, if tracking the PGV and PGA measurements in aggregate, are 79% (BB), 77% (DW), 71% (SG), 56% (JF), 50% (TR, PY, and RA). Collectively, these results indicate that extrapolation from one location to regions within only a few kilometers away could be in error.

If we were to evaluate the PGV and PGA results separately, only the BB (PGA) and JF (PGA) data show consistent results across all stations (Tables S4a-b). Five of the arrays are close to consistency, with only one station reporting maximum ground motion from a different earthquake. Four of these five networks (JF, DW, TR, and RA) show the outlier station is at the edge of the array, which is more intuitive than in the middle of the network, as observed within the SG network (station SGBS2 mid-network). A potential explanation for the oddball SG station is that the SG array sits atop basin structures (Johnson et al., 2020; Share et al., 2020), so basin resonance effects might be responsible for this behavior as previously mentioned.

Because of the small footprints of these seven small aperture arrays, we expect that the largest PGA and PGV reported by each station within an array would be generated by the same earthquake. Surprisingly, this was only observed for the BB and JF array's PGA measurements (Table S4a-b). Differing from this, the maximum PGA values reported by the 13 stations in the DW array were generated by 3 different earthquakes and the PGA recorded at the 12 stations in RA array were generated by 4 different earthquakes. For the PY network, the maximum PGA and PGV were generated by three different events across the 13 stations, where the same three events were identified in the PGA and PGV results. The maximum PGA for the four stations in the TR network identified two earthquakes. The largest PGV measurements at the four stations in the TR array pinpoint four different quakes. The TR array is the longest (3 km, compared with less than 0.2 km for some of the other arrays, see Table S2), so it is the most likely array to show deviations between the results. But it is surprising that all four stations report different quakes as producing the largest amplitudes. Collectively, this indicates that care should be taken when extrapolating large ground motions recorded at one station to nearby regions, and that even within a 3 km extrapolation could be in error.

4.6.1 BB array: Ground Motion Dichotomy Across the Fault

We also find a spatial consistency in the BB (PGV) array results, where stations to the southwest of the fault (BB01, BB02, BB03) report an M3.63 earthquake at azimuth 59° as producing the largest ground motions. In contrast, the northeast stations (BB04, BB05, BB06, and BB07) report an M3.08 earthquake at azimuth 117°, generating the largest ground motions. Thus, the largest ground motions reported on the southwest side of the fault were from seismic waves arriving approximately perpendicular to the fault, and those on the northeast side from seismic waves arriving approximately along fault. We address the question: Why do ground motions from an M3.08 earthquake recorded at stations on the northeast side of the BB array (BB04, BB05, BB06, and BB07) produce ground motions on par with or higher than an M3.63 event located at similar depths and distances, but a different azimuths from the BB array (Figure 6)?

We first theoretically establish how different the ground motions should be between the M3.08 and M3.63 events, which have similar distances and depths. To do so, we use the seismic moment ratio of the two events:

$$\frac{10^{(1.5\times 3.63)}}{10^{(1.5\times 3.08)}} = 10^{(1.5\times 0.55)} = 10^{0.825} \approx 6.68 \qquad (3)$$

This shows the M3.63 event should, on average, produce ground motions approximately 6.68 times larger than the M3.08 event. This is just a first-order estimate, there are numerous other factors that could alter this estimate including data quality, stress drop, source directivity, site or path conditions, and focal mechanism effects. Additional smaller events could contaminate the waveform's coda and elevate the amplitudes; however, there is no evidence of such contamination based on the ComCat catalog (U.S. Geological Survey, 2017).

4.6.2 BB array: signal-to-noise ratio (SNR)

We evaluate signal-to-noise ratio (SNR) across the fitting band (0.5–25 Hz) using the metric snr_pct, which is the fraction of frequency bins where signal amplitude exceeds noise by a factor of 2.5 (Kilb et al., 2012). Waveforms with snr_pct < 0.5 are flagged and excluded. For the M3.63 event, excluded waveforms include all components at KLCI and TMSP and the vertical component at PRAN, seven waveforms in total. For the M3.08 event, exclusions include the vertical components at KLCI and PRAN, two waveforms in total. Despite being

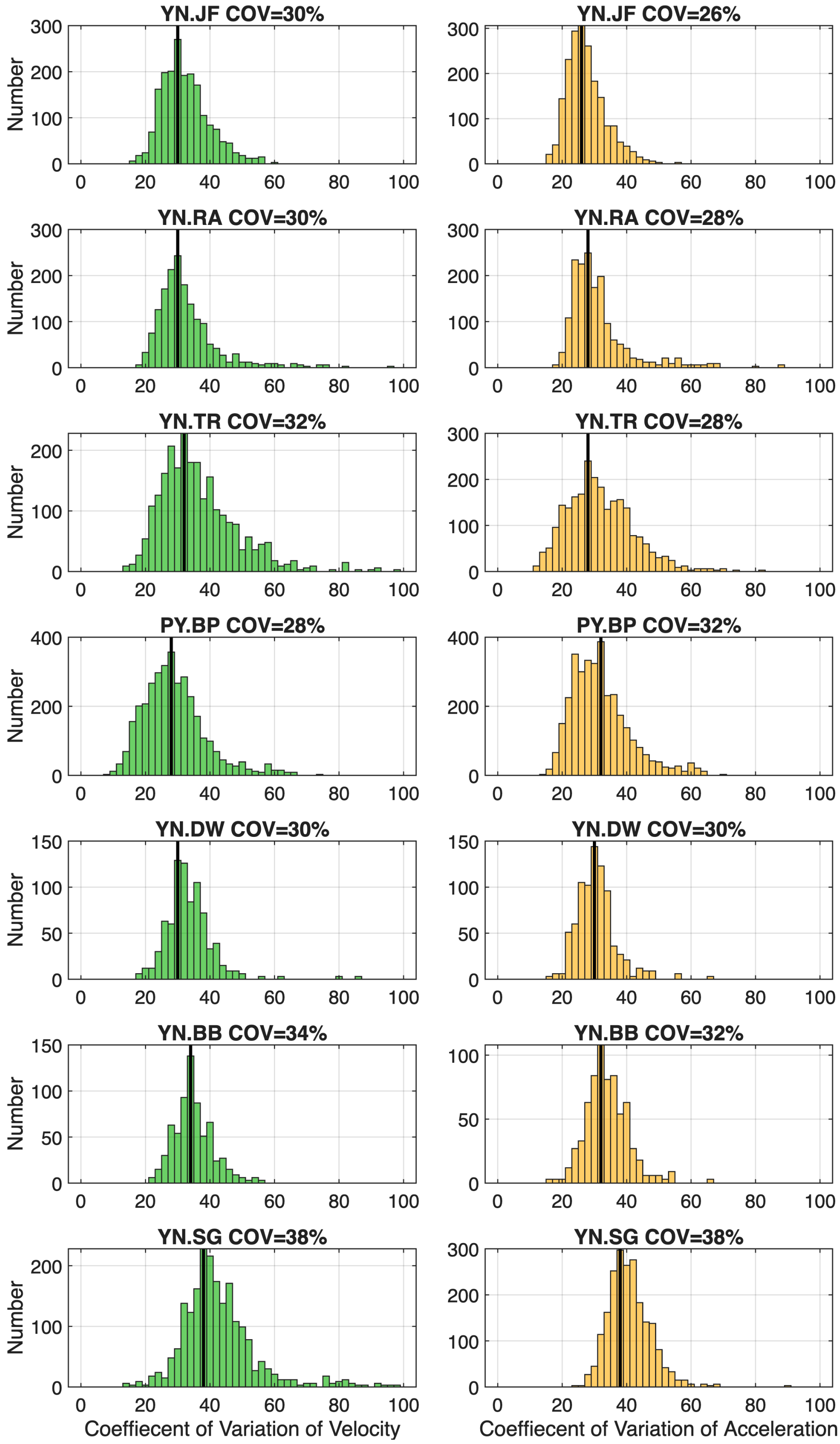

Figure 5 Coefficient of variations (COV; standard deviation/mean) distributions for PGV (left, green) and PGA (right, orange). The mean percentages (vertical lines) deviate by no more than 4% between the PGV and PGA estimates for each network (i.e., compare values in the titles of each row). We assume this 4% bounds the uncertainties. The largest COV percentages are observed within the SG array, showing variations of 38%. This means that the peak ground motion measured at one station in the array can be 38% different from that measured at another station in the same array.

the smaller event, M3.08 achieves high SNR across all stations, with 29 of 42 waveforms (69%) reaching perfect snr_pct scores (snr_pct=1.0). In contrast, M3.63 achieves zero perfect scores across the same 42 waveforms.

At the BB array specifically, the contrast is even more

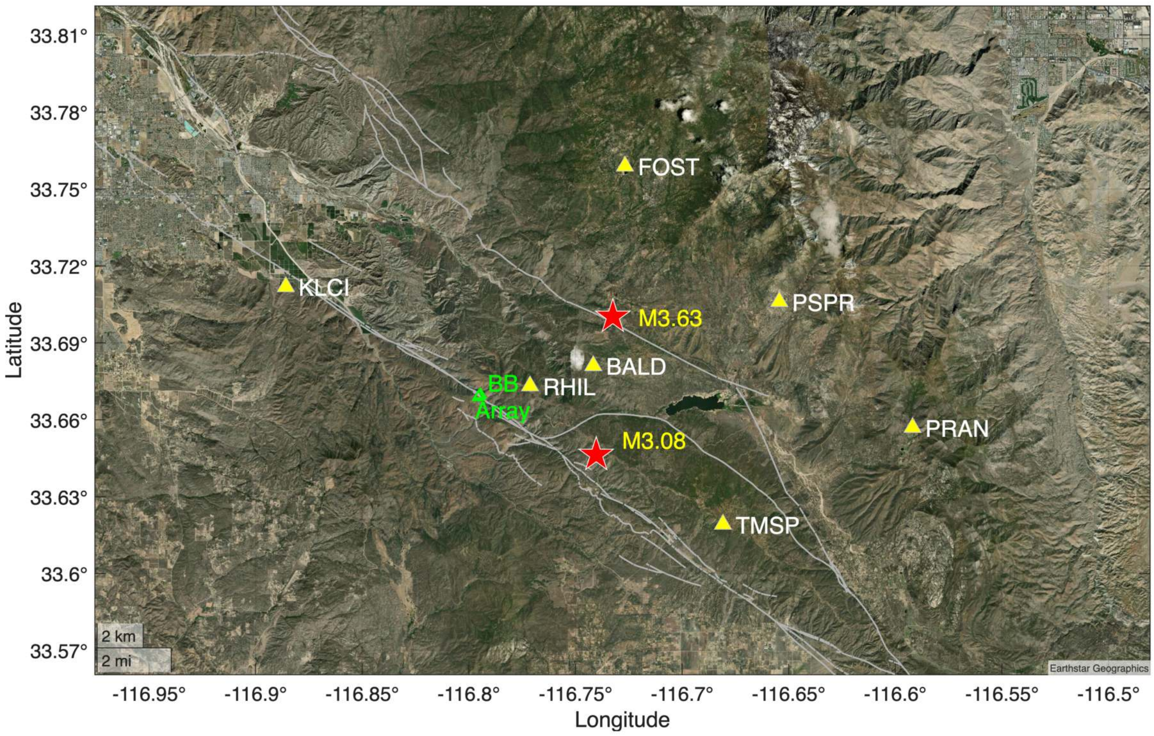

Figure 6 Map of the 14 stations in the BB array study. These include the seven BB stations (green triangles, labeled) and seven additional stations nearby (yellow triangles). Also included are select earthquakes (red stars, labeled with magnitudes) along the San Jacinto fault zone. Fault traces (grey lines) are from the Quaternary Fault Database (U.S. Geological Survey, 2004). Satellite imagery courtesy of Earthstar Geographics.

pronounced. The M3.08 achieves a perfect score for all 21 BB waveforms (7 stations $\times$ 3 components, 100%). Notably, the M3.63 achieves zero perfect scores at the BB array, with snr_pct values ranging only 0.70–0.99. The consistently lower SNR of the larger M3.63 event at comparable distance is consistent with the M3.08 radiated relatively more energy toward the BB array.

4.6.3 BB array: Seismic Moment

We test whether the assigned catalog magnitudes are in error by examining the seismic moment M_0 derived from the low-frequency plateau of the displacement spectra. Only data with SNR_pct greater than or equal to 0.5 are used in the analysis. M_0 is related to moment magnitude M_w by

$$M_w = \frac{2}{3}\log_{10}(M_0) - 6.07,$$

where M_0 is in N·m (Hanks and Kanamori, 1979). We use M_w as a proxy for the local magnitude M_L, as the two are empirically well-correlated (Hanks and Boore, 1984).

We find the rank ordering is as expected, showing a larger mean M_0 for the M3.63 event (2.43×10^{14} N·m, M_w from the spectra = 3.52) than the M3.08 event (1.17×10^{14} N·m, M_w from the spectra = 3.31). The spectral M_w estimates are separated by only 0.21 magnitude units, compared to 0.55 units in the M_L catalog values. But this discrepancy is not unexpected, as local and moment magnitude are measured by different methods and can diverge for moderate earthquakes (e.g., Boore, 1989).

The ratio of the spectral mean moments (M_0 for M3.63 divided by M_0 for M3.08 = $2.43 \times 10^{14}/1.17 \times 10^{14} \approx 2.1$) is, however, substantially smaller than the ratio implied by the catalog magnitudes. Applying the same moment-magnitude scaling relation used above ($M_0 \propto 10^{1.5M}$), the catalog M_L values, which differ by 0.55 units, imply a moment ratio of $10^{(1.5\times0.55)} \approx 6.7$, which is roughly three times larger than the ratio observed in the spectral moments. This discrepancy suggests the two events are closer in source size than their assigned catalog magnitudes indicate. Because the rank ordering of spectral M_0 is consistent with the catalog, the M3.08 source moment is not anomalously large, and magnitude error alone cannot explain why the smaller earthquake produces larger PGV at most stations. This suggests the excess ground motion likely originates above the corner frequency, possibly reflecting differences in stress drop or rupture directivity.

4.6.4 BB array: Stress Drop

We process data from 14 BB stations (three components: R, T, Z) to produce M_0 and fc estimates with uncertainties derived from trade-off curves (Kilb et al., 2012). We explore trial corner frequencies spanning 0.5–25 Hz, where 25 Hz corresponds to the upper limit of reliable signal-to-noise ratio for these data. Displacement spectra are fit to a (Brune, 1970) omega-squared source model with attenuation represented by the parameter kappa, which is estimated simultaneously with Ω_0 and fc at each trial corner frequency. The long-period spectral level is corrected for geometrical spreading, free-surface amplification, average S-wave radiation pattern (0.55), and S-wave amplitude partition onto a single horizontal component ($1/\sqrt{2}$, assuming equal energy on radial and transverse).

Independent spectral fitting yields poorly constrained corner frequencies for both events. The M3.63 yields no well-constrained fits on either horizontal component. For the M3.08 event, only 1 of 28 horizontal measurements passes the quality criteria. The single passing fit (BB01-T) yields a 75% confidence interval of ~5–25 Hz, with the upper bound at the edge of the analysis band and the trade-off curve minimum poorly defined. This is consistent with fc at or above 25 Hz rather than a well-resolved lower limit. The dominant failure mode is insufficient spectral roll-off within the 0.5–25 Hz analysis band. This result is itself informative, suggesting fc for both the M3.08 and M3.63 events is likely at or above the upper limit of the analysis band (25 Hz). Because stress drop scales as fc^3, even modest uncertainty in fc translates to large uncertainty in stress drop (Brune, 1970). We conclude that robust fc and stress drop estimates are not possible for these data.

4.6.5 BB array: Waveforms

Within the BB array, horizontal amplitudes show a clear southwest-to-northeast gradient. BB01, the only BB array station outside the assumed fault zone, is borderline: M3.63 leads M3.08 by ~21% on R, while the two are essentially equal on T (<1%). BB02 most clearly favors M3.63, which exceeds M3.08 by 21–72% on R and T. From BB03 northeastward, M3.08 exceeds M3.63 on all horizontal components except BB04 R, where M3.63 leads by 30%, with M3.08 exceedances reaching 3–72% at individual stations. In no case does any component pair approach the 6.7× amplitude ratio expected from moment scaling alone (see supplemental Figure S9).

At the non-BB stations, PRAN shows M3.63 dominance, with ratios of 0.40 and 0.34 on R and T (-66%; Figure 7, panel e), broadly consistent with M3.63's greater seismic moment. RHIL shows component-dependent behavior: M3.08 barely exceeds M3.63 on the radial (~3%) while M3.63 dominates on the transverse (~31%; Figure 7, panel g), likely reflecting differences in SV and SH radiation patterns at that azimuth. PSPR is a dramatic exception, with M3.08 exceeding M3.63 by +306% on T (Figure 7, panel a), discussed in detail below.

4.6.6 BB array: Directivity

Earthquake source processes can elevate ground motions in two fundamentally different ways: anomalously high stress drop or rupture directivity. If high stress drop is at play, elevated energy would be distributed uniformly across all azimuths. The signature of rupture directivity differs from this, showing amplifying ground motions in the direction of rupture propagation while reducing ground motions in the opposite direction. Next, we investigate which mechanism better explains the large M3.08 ground motions recorded at the BB array.

For the M3.08 event, the T-component velocity waveforms and displacement spectra reveal a stark amplitude contrast between signals recorded by the BB array (AZ ~297°) and TMSP (AZ~119°), showing peak amplitudes that differ by roughly an order of magnitude (Figure 8). This asymmetry is consistent across all seven BB stations, which track each other closely in both waveform shape and spectral level, ruling out single-station site effects. TMSP shows a weak S-wave arrival with amplitudes roughly an order of magnitude below the BB array. The azimuthal amplitude asymmetry is not explained by the M3.08 focal mechanism radiation pattern, which predicts nearly equal S-wave amplitudes at TMSP and the BB array (see Focal Mechanisms section). We therefore attribute this asymmetry to rupture directivity of M3.08 toward the BB array.

Although the primary explanation for the observed amplitude enhancement at BB04–07 relative to BB01 is forward directivity of M3.08 toward the BB array, a contribution from fault-zone trapped waves (FZTW) cannot be excluded. The location of M3.08 within the fault zone makes it an efficient source for guided SH waves in the low-velocity fault core (Li et al., 1990; Ben-Zion and Aki, 1990), which would produce preferential transverse-component amplification at the in-fault stations BB04–07 relative to the off-fault control station BB01. The observed amplitudes, however, show radial exceeding transverse at most stations, which is inconsistent with a dominant FZTW contribution and more consistent with a P-SV directivity effect. The short aperture of the BB array precludes a more definitive separation of these contributions.

4.6.7 BB array: Focal Mechanisms

Ground motion amplitudes are modulated by focal mechanism radiation patterns, which vary across the focal sphere by up to a factor of ~4 for S waves (Aki and Richards, 2002). We compute theoretical S-wave radiation amplitudes at each station using the analytical double-couple radiation pattern expressions for SV and SH waves, combined into a single S-wave radiation coefficient, $F_S = \sqrt{F_{SV}^2 + F_{SH}^2}$), which depends on the source strike, dip, and rake together with the station azimuth and takeoff angle. Both events have similar hypocentral distances from the BB network, with source-to-BB-array azimuths of ~297° for M3.08 and ~239° for M3.63, and takeoff angles of approximately 20° for both events.

For each station, $|F_S|$ is evaluated at the station azimuth and per-station takeoff angle derived from hypocentral geometry (see supplemental Table S5). Observed PGVs are distance-corrected and taken as the mean of the radial and transverse components, where both predicted and observed values are expressed as M3.08/M3.63 ratios. Figure 9 shows the per-station observed PGV ratio versus the predicted F_S ratio, where stations plotting on the 1:1 line are fully explained by

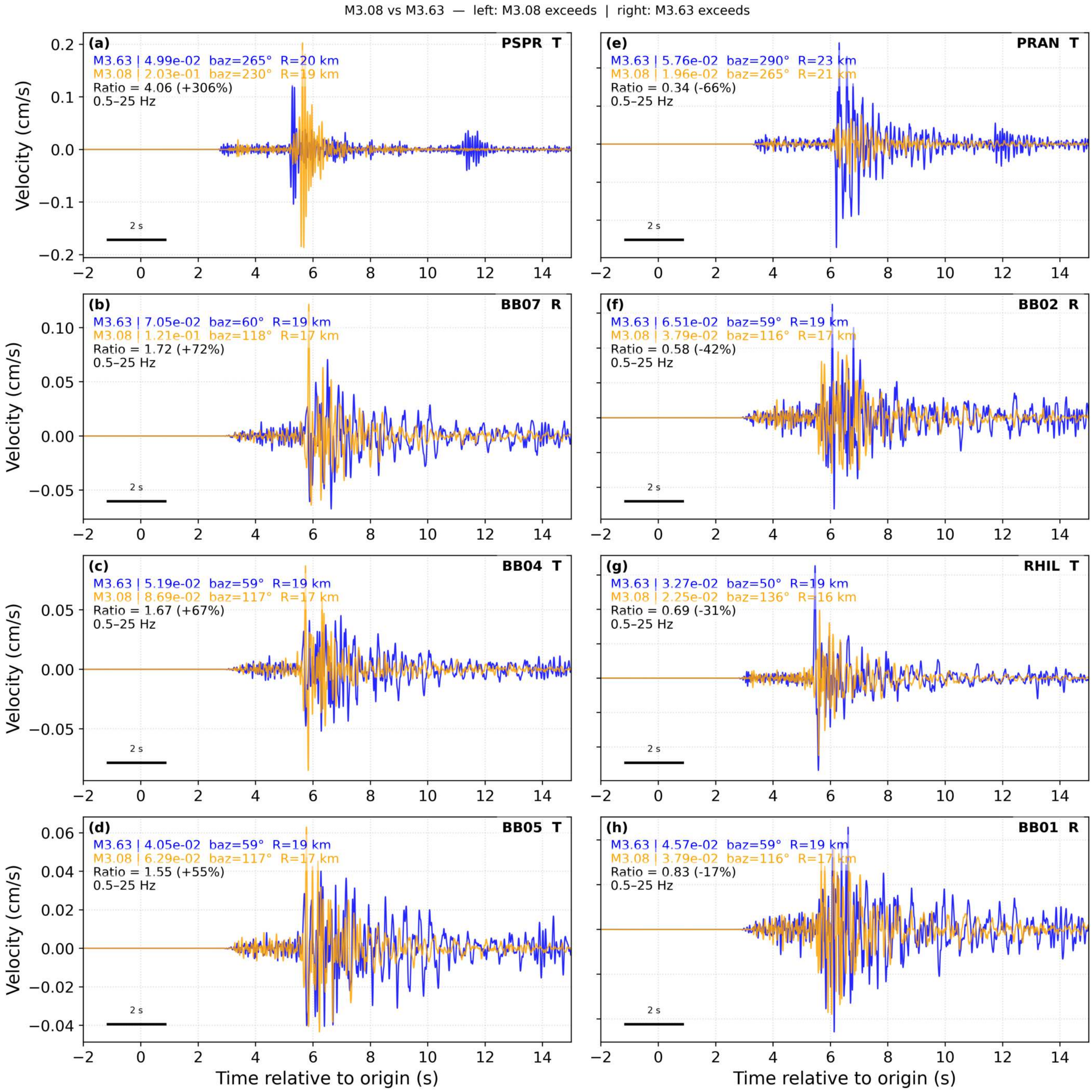

Figure 7 Selected velocity waveform pairs comparing M3.08 (orange) and M3.63 (blue), bandpass filtered 0.5–25 Hz. Left column (a–d): stations where the smaller M3.08 event anomalously exceeds M3.63, including PSPR and three BB array stations. Right column (e–h): stations where M3.63 dominates as expected. Panels within each column are ordered from most to least extreme amplitude contrast. Note that y-axis scales differ between panels. Text insets give peak ground velocity (PGV), backazimuth (baz), and hypocentral distance (R) for each event at each station.

the focal mechanism.

At the BB array azimuth, the predicted F_S ratio (M3.08/M3.63) is 0.55, meaning that M3.63's focal mechanism produces ~82% ($1/0.55 = 1.818$; $(1.818 - 1) \times 100 = 82\%$) larger S-wave radiation amplitude toward the array than M3.08 (Figure 9). The focal mechanism therefore predicts M3.08 should be the weaker of the two events at the BB array. Despite this disadvantage, observed PGV ratios on the horizontal R and T components show M3.08 equaling or exceeding M3.63 at 12 of 14 BB station-component pairs (ratio ≥ 0.80; note that the ~18% hypocentral distance difference between events has not been corrected for, but does not change the qualitative conclusions). The clearest exceptions are BB02-R (ratio=0.58) and BB04-R (ratio=0.70), both on the radial component at the southwestern end of the array. This southwest-to-northeast amplitude gradient within the array cannot be explained by focal mechanism effects, which are expected to be uniform across the ~180 m aperture.

At non-BB stations, results are more mixed. PRAN, RHIL, and FOST plot near the 1:1 line, within the $\pm 20\%$ limits, suggesting their amplitude ratios are broadly consistent with focal mechanism predictions. BALD

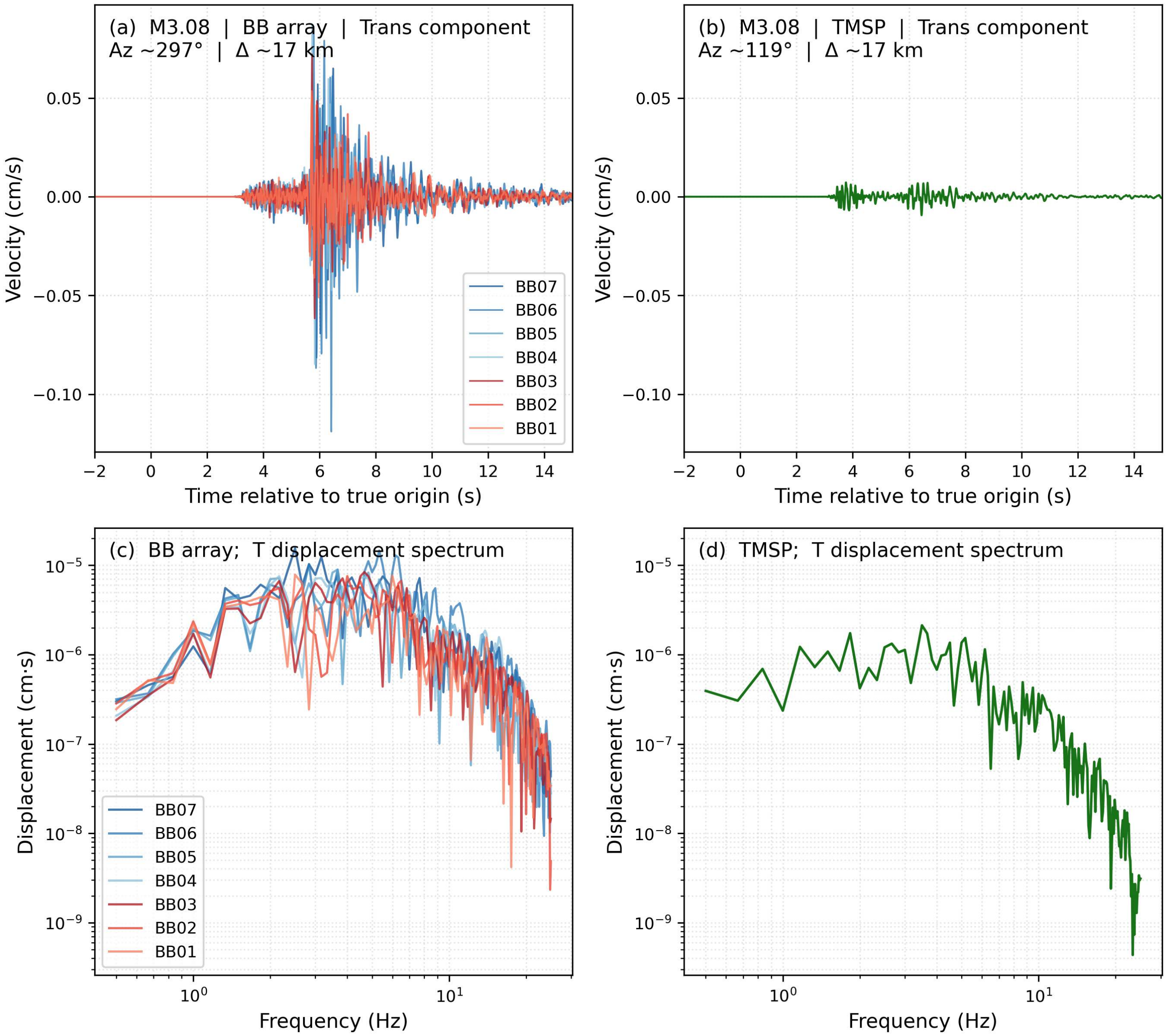

Figure 8 M3.08 directivity investigation using a station-pair on nearly diametrically opposite azimuths (separated by ~178°). (a) Transverse component velocity waveforms at the seven BB array stations (BB01–BB07), colored in red hues at the southwest end (BB01–03) to blue hues at the northeast end (BB04–07). (b) As in (a) but for velocity waveform at TMSP. No distance correction was applied because the stations are located at similar distances from the source. The BB array amplitudes exceed TMSP by well over an order of magnitude. (c, d) Corresponding transverse component displacement spectra, showing that the amplitude disparity persists across the full frequency band. The contrast supports preferential energy radiation from M3.08 toward the BB array, which cannot be explained by focal mechanism effects.

plots above the $\pm 20\%$ limit, indicating M3.08 is somewhat stronger than the radiation pattern alone predicts. TMSP is an exception in the opposite direction: despite a high predicted F_S ratio (~1.57, favoring M3.08), the observed PGV ratio (~0.88) falls below the $\pm 20\%$ limit. This is consistent with M3.08 being in the anti-directivity direction from that station as noted above. Notably, the M3.08 radiation pattern predicts comparable absolute S-wave amplitudes at TMSP (~119°) and the BB array (~297°), confirming that the order-of-magnitude PGV contrast between these azimuths is not a radiation pattern effect.

PSPR plots far above the $\pm 20\%$ limit, with an observed PGV ratio of 3.43, which is more than five times larger than the focal mechanism prediction. Radiation pattern effects, therefore, cannot account for the anomaly. Using four reference earthquakes in the region (M1.87–2.25; March–July 2013), we compare spectrograms from PSPR with those from BALD, located ~9 km to the west. All four events show that the T-component of PSPR is consistently larger than the T-component of BALD by a factor of 5–17. This is consistent with persistent site amplification at PSPR. Consistent with that hypothesis, the anomalous T amplitude (2.03 mm/s) is equivalent to the ground motion expected from an M_L ~2.5 earthquake 0.5 km from PSPR. Yet, no such event appears in the ComCat catalog (U.S. Geological Survey, 2017), and there is a lack of a subsequent earthquake signal at any of the nearby stations, which confirms the energy is not coda contamination from a nearby microearthquake.

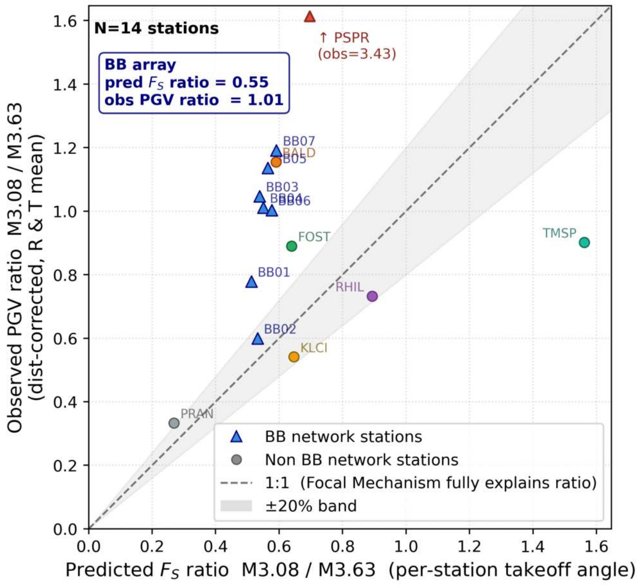

Figure 9 S-wave radiation pattern analysis for the M3.08 (strike=295°, dip=39°, rake=132°) and M3.63 (strike=146°, dip=61°, rake=−150°) events (SCEDC, 2013). PGV values are distance-corrected, and the predicted F_S ratio uses per-station takeoff angles computed from event geometry. Agreement with the 1:1 line indicates that the difference in radiation pattern between the two focal mechanisms fully accounts for the observed amplitude ratio. Deviation above the 1:1 line indicates M3.08 is relatively stronger than the focal mechanism predicts, whereas deviation below indicates it is relatively weaker. BB array stations (blue triangles) plot well above the 1:1 line (observed ratio 1.01 vs. predicted 0.55), indicating M3.08 ground motions at BB are nearly twice as strong as the focal mechanism alone predicts. PSPR has an observed PGV ratio of 3.43, well above the plot range (an upward-pointing marker at the top of the figure indicates its clipped position). KLCI is included here but has low signal-to-noise ratio for M3.63 and is excluded from waveform comparisons. No stations were excluded for proximity to a nodal plane.

4.7 Spatial Patterns of Peak Amplitudes Across Faults

The seven array locations can be categorized as arrays that do not traverse a fault (TR and PY; Figures 7 and A4), arrays that traverse a fault that is considered a relatively simple single-strand fault (BB, DW, JF, and RA see Figures 1, A2, A3, and A5), and arrays deployed within a complex faulting regime consisting of more than one fault strand within relatively close proximity (SG; See Figure 6). We focus on the simple fault strand category and assess how the ground motion peak amplitudes vary spatially across these four arrays. We limit these data to events recorded at all stations in the array that have all 3-components of data. We eliminate data that do not meet these requirements to ensure that our comparisons are consistent.

Our results show an intriguing feature in the RA and JF spatial distributions of peak ground motion amplitudes (Figures 10a-b). Data from both arrays show lower amplitudes within the fault core that increase outward toward the fault zone edges. These peak amplitudes then fall off to the smallest amplitudes at distances outside the fault zone. These amplitude variations produce an 'M' shape in the peak amplitude distributions. The peak amplitude distribution for the BB array (Figure 10c) is challenging to evaluate because the length of this array is much shorter than the other arrays. The JF and RA arrays have lengths of 0.37 km and .46 km, respectively, whereas the BB array is only 0.18 km long (see Table S2). That said, the general trend of the BB peak amplitudes tends to increase from the most southwestern station (BB01) toward the most northeastern station (BB07). The exception to this rule is the vertical BB04 component. However, this difference is not outside the error ranges and should not be overinterpreted. The spatial variability in the distribution of peak amplitudes in the DW array data (Figure 10d) differs from the patterns found in the other three networks (Figures 10a-c). The DW distribution is subtle, not showing significant spatial changes across the array.

5 Discussion

Key in this work was data quality control, which included removing potentially overprinted signals (i.e., event pairs within 5 km and 5 minutes of each other), SNR restrictions, and tests for potentially non-viable data that produce signals outside (too high or too low) of empirically expected values. Our tests for non-viable data revealed that within the RA array data, ground motions generated by traffic along nearby roadways, within ~100 meters of the recording station, can swamp signals from distant, smaller earthquakes (>80 km; ~M_L 2). These road-noise-contaminated waveforms are not likely to be caught by the SNR tests. Following a precautionary approach, data collected within ~100 meters of high-traffic roadways should be excluded (Meng et al., 2021).

For each network, differences in the log of the observed to empirical ground motion ratios are not random or skewed, primarily showing a normal distribution of values (Figure 4). These normal distributions suggest that the site term is the dominant property dictating ground motions, not the source or path terms. We expect these normal distributions for two reasons. First, we do not expect source terms to dominate because the catalog contains primarily small-magnitude events, and in turn, most events can be considered point sources. The second reason is the small footprints of these arrays that, in theory, should be measuring very similar ground motions (Johnson et al., 2020; Pischiutta et al., 2024; Meng and Ben-Zion, 2017).

Our results indicate that even for these small footprint arrays (<3 km length), a single earthquake can produce highly variable ground motions across the array. This is substantiated by the results: (1) the same

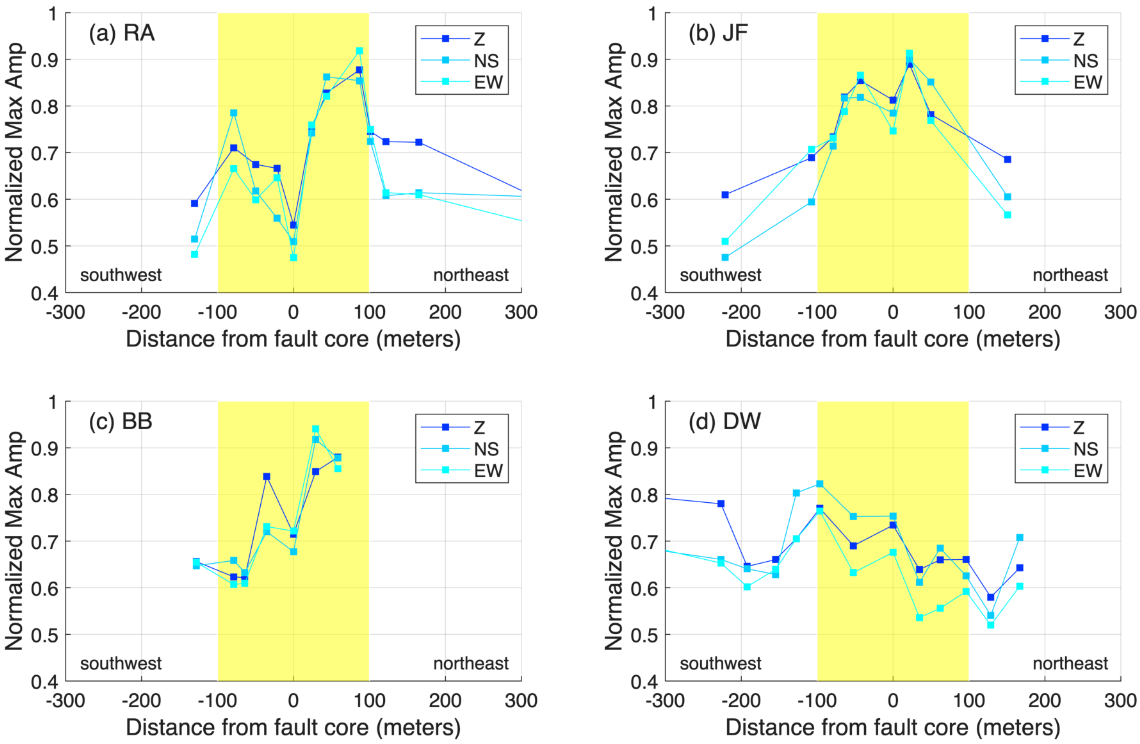

Figure 10 Spatial variation of peak ground motions at arrays (a) RA, RA05 assumed to be at fault core (see Figure 5) (b) JF, JFN1 assumed to be at fault core (see Figure 3); (c) BB, BB05 assumed to be at fault core (see Figure 1); and (d) DW, DW12 assumed to be at fault core (see Figure 2). Distances are measured from the fault core running perpendicular to the fault strike. These data are restricted to events recorded at all stations in the array that contain all three components of data. Different components of data are color-coded and show similar behavior. The yellow shading encompasses the approximate width of these faults, at ± 100 meters from the fault core (Pischiutta et al., 2024). Note the RA and JF distributions show an “M” pattern, where the fault core amplitudes are smaller than the fault zone edges, and ground motions are reduced outside the fault zone. There is a hint of the “M” shape in the BB data, but the spatial extent of this array is not wide enough to confirm this is a true feature. DW does not exhibit the “M” pattern, differing the most from the distributions presented from the other three arrays. These are preliminary results as the exact location and width of these faults are estimates.

earthquake does not always generate the largest ground motions recorded at stations within an array (see Table S4), and (2) ground motion variability measured by the coefficient of variations (standard deviation/mean) is relatively high for all arrays at ~26%-38% of the mean (Figure 5). Near the JF, RA, and BB arrays, we expect the variability to be driven primarily by low-velocity zone contrasts and structure (i.e., Figure 10; symmetrical properties and strength contrasts). Whereas near the SG array, which traverses a series of faults, we anticipate that ground motion differences are dictated by basin resonance. Past studies support this resonance hypothesis (Johnson et al., 2020; Share et al., 2020; Yeh and Olsen, 2023; Qin et al., 2017), and this theory is also consistent with the SG data producing the largest coefficient of variations of all arrays.

The data most similar to the empirical expectations were recorded by the off-fault TR array (see Figure 4), and the off-fault PY array recorded smaller ground motions than empirically expected. Conversely, the five along-fault network arrays (BB, JF, SG, RA, and DW; listed in order from largest to smallest differences) recorded ground motions below the empirical expectations. These findings suggest fault zone influences tend to increase ground motions. The reason the BB array exhibits the largest difference from the empirical explanation might be because it has the largest low-velocity zone with the largest velocity contrasts. But, we expect the reason might be more complicated and depend on the orientation of the incoming waves and their frequency content (Schliwa et al., 2025).

Of the seven networks, the largest PGV and PGA coefficient of variation measurements are 38% from the SG network (Figure 5). Johnson et al. (2020) found deviations of 22% for the Sage Brush Flat 2D array, which is co-located with the SG linear array examined in this work. The differences in these variations of 38% and 22% for this study and the Johnson et al. (2020) study, respectively, are not surprising because of the difference in the durations of the recordings (~13 years vs. ~1 month), the lack of horizontal recordings in the Johnson study, and that the 2D network configuration had smaller station spacing (1,108 geophones, station spacings 10 - 30 m) that covered multiple basin structures. In contrast, our study examined data from a linear array with only seven stations.

Two events generate the largest ground motions within the BB PGV data: the M3.63 (southwest stations BB01–BB03) and the M3.08 (northeast stations BB04–BB07), where seismic waves arrived perpendicular to the fault (azimuth ~59°) and along-fault (azimuth ~117°), respectively. Peak ground motions at the northeast stations are larger (≥0.25 cm/s) than those at the southwest stations (≤0.22 cm/s; Table S4a). A study by Pischiutta et al. (2024) found that BB stations northeast of the fault show significant increases in HVSR amplitude, with amplifications particularly enhanced for seismic waves arriving from azimuths of 100–150°, whereas southwest stations do not exhibit such increases. Our observations are consistent with this: northeast stations show enhanced amplitudes for waves arriving at ~117° (within the 100–150° range), while southwest stations record their largest ground motions from a different earthquake at a different azimuth (~59°).

The BB array results establish that ground motion amplitudes are both azimuthally dependent and spatially asymmetric across the fault. Sections 4.6.2–4.6.7 systematically rule out several potential causes including SNR artifacts, magnitude error, anomalous source moment, and focal mechanism effects. Instead, rupture directivity of M3.08 toward the BB array is identified as the primary explanation. An asymmetric low-velocity zone beneath the BB array, with smaller amplitudes and shallower depths below the southwest stations and larger amplitudes and greater depths below the northeast stations (Share et al., 2019), may also contribute. The longer Blackburn Saddle array (Share et al., 2018) could, in future work, provide data to more thoroughly test these interpretations.

The pronounced "M" ground motion spatial patterns (see Figures 10a-b) are similar within the RA and JF data. Past studies have identified symmetrical low-velocity zones within relatively narrow fault zones in these regions (e.g., Qiu et al., 2017; Wang et al., 2019; Zigone et al., 2019), noting that these configurations can generate fault zone trapped waves (FZTW). We posit that the multiple reflections of the FZTW add constructively at the edges of the fault zone and destructively at the center core of the fault zone. The smallest ground motions observed at stations farthest from the fault are a consequence of being far enough away from the fault core, and in turn, low-velocity zones, that they are not influenced by these structures. For the DW data, we attribute the lack of an "M" signature (Figure 10d) to the lack of a low-velocity zone beneath DW, or perhaps frequency-dependent or a very muted low-velocity zone in comparison with those beneath the JF and RA arrays (Qiu et al., 2017; Yang et al., 2014; Wang et al., 2019; Zigone et al., 2019; Pischiutta et al., 2024).

Low-velocity zones within fault zones tend to increase ground motions (Cormier and Spudich, 1984). Given this, the observed variability of ground motions can guide estimations of the strength and symmetry of low-velocity zones. Comparing spatial ground motions from the RA, JF, BB, and DW arrays, we can generally conclude that there are likely symmetrical low-velocity zones beneath the JF and RA arrays, an asymmetrical low-velocity zone beneath the BB array, and an absent or very muted low-velocity zone beneath the DW array.

One factor that can make spatial extrapolations of peak ground motions from one location to nearby locations challenging is that earthquake-generated peak ground motions can be frequency band dependent (i.e., Rathje et al., 1998; Chatterjee et al., 2024). The filter used in this work is relatively wide (0.5-25 Hz), and we did not study the intricacies of frequency dependencies. The Pischiutta et al. (2024) work found that data from the JF and RA arrays had similar amplified frequency distributions, showing greater amplification factors for seismic waves less than 1 Hz along fault, and 1-5 Hz across fault, and the BB array amplification factors were largest in the ranges 1-5 Hz along fault. They also concluded that the JF, RA, and BB arrays have similar trapped wave orientations that are absent in the DW array data. This last conclusion is consistent with our ground motion findings in Figure 10.

Using a large amount of data to explore geoscience concepts is a growing field, of which small aperture seismic arrays are a growing subset of the new projects (Ben-Zion et al., 2015; Li et al., 2018; Mordret et al., 2018; Qiu et al., 2021; Arrowsmith et al., 2022; Pischiutta et al., 2024; Lentas et al., 2026). A study of small-aperture arrays in Iceland found that in regions of large geologic and topographic variability, ~57% of ground motion variability can be attributed to site terms alone, and even in regions where the geologic structure is similar and topography variations minimal that site terms can still produce ~13% of ground motion variations (Rahpeyma et al., 2019). A study from the Sage Brush Flats region in southern California compared surface ground motions with ground motions from a 148-meter deep borehole and found that surface recordings can be 3-10 times larger than borehole recordings (Johnson et al., 2020). These results are similar to what is found in this study, suggesting that ground motions generated by a single earthquake can be spatially very heterogeneous within a small region.

6 Conclusions

This work measures ground motions (PGV and PGA) of M_L 2.5+ earthquakes within 150 km of the centroid of seven small aperture arrays in southern California. Each of these seven catalogs contained a year or more of data and consecutive events were required to have space and time separations greater than 5 km and 5 minutes. The SNRs were required to be 2.5 or higher (see supplemental Figure S3). This data quality vetting flagged primarily data from the SG network (~6% of the waveforms) and to a lesser extent the RA network (~4% of the waveforms), TR network (~2% of the waveforms), and JF network (~1% of the waveforms). For the other arrays (BB, DW and PY) <1% of the waveforms were flagged. We also compared the SNR histogram distributions from each station within the individual networks to identify anomalies at individual stations. The SNR distributions are similar for DW, JF, BB, and PY network stations, but dissimilar for the RA, SG, and TR networks (Figures S2-S3). We found the dissimilar results resulted from instrumentation problems over relatively short durations. This data quality vetting is very powerful, indicating that data quality can easily be assessed by comparing the SNR distributions for similar earthquakes across the different stations within a small aperture array.

The peak ground motions (PGV and PGA) observed at each station in the seven networks have a consistent trend compared to the empirical estimates (see Figure 4). Observed ground motions recorded at networks within the fault system (BB, DW, JF, RA, and SG) produce larger-than-expected ground motions. In contrast, off-fault networks produce ground motions as expected (TR) or slightly lower than expected (PY). Consistent with past studies, this suggests that, generally, fault zone properties tend to elevate ground motions, not reduce them (Pischiutta et al., 2024).

We also conducted non-viable waveform tests by flagging and examining data that were either substantially larger or smaller than empirically expected. These flagged outliers represent less than 1% of these data, suggesting that data used in this study are of high quality and that the overprinting and SNR tests identify most of the suspect data. Ultimately, only 350 waveforms were deemed non-viable (Kilb and Vernon, 2025c). Many of these non-viable data were recorded by the RA array for relatively small and distant earthquakes (~M2, >80 km) that produced relatively small ground motions. These signals were so small that larger signals from cars and trucks passing along the nearby roadway (within ~100 meters) corrupted the earthquake signals, suggesting caution should be taken when using data near busy roadways.

On a more granular level, our work suggests that low-velocity zones can influence the distribution of ground motion behavior. For relatively simple faults with low-velocity zones oriented symmetrically with respect to a single fault strand, as near the RA and JF networks, ground motions are reduced directly at the fault core, elevated at the fault zone edges, and the smallest at regions more distant from the fault. This creates an "M" shaped pattern in the ground motion distributions (Figures 10a-b). In regions with non-symmetrical low-velocity zones, ground motions become amplified above the strongest and deepest velocity anomalies, as observed in the BB array data (Figure 10c). The lack of strong ground motion variability across an array suggests that if low-velocity anomalies exist in the region, they are relatively muted. Collectively, these observations indicate that simply observing the variability in ground motions across an array can help infer the existence, strength, and symmetry of low-velocity zones.

One of the most surprising findings in this work was that the largest ground motions recorded by stations within a single array were not always generated by the same earthquake (see Tables S4a-b), as might be expected for such small aperture arrays. If looking at the PGV and PGA results separately, only the BB (PGA) and JF (PGA) show 100% consistency. Many other configurations show only one station out of step with the others, and that station is typically at the edge of the network. However, that is not the case for the SG (PGV) data, where the anomalous station is mid-network. We attribute this difference in the SG data to basin resonance within the region. Notably, for the TR (PGV) data, the four events that produced the largest ground motions at the four stations all differed.

In summary, we return to our original question – to what extent can data recorded at one station be extrapolated to nearby regions? Past work indicates that the variability can be quite large, even within small footprints (e.g., Rahpeyma et al., 2019; Johnson et al., 2020). In this work, for arrays with small diameters of 3 km or less (Table S2), the variability in PGV and PGA measurements has a variation coefficient between 26% and 38%. This means that ground motions recorded at one station in the array can be 26%, or even 38%, different from those recorded at another station in the array for the same channel. These differences should be considered more the norm than the exception, especially within regions that contain basin structures and regions close to fault zones.

Acknowledgments

We thank those who planned and deployed these networks and collected and cataloged these data for public distribution. The project benefited from multiple email discussions with Robert Weekly about data acquisition from the IRIS repository and scientific discussions with Hongfeng Yang. We also thank Yehuda Ben-Zion for helping frame the research project proposal and Paul Dean and Katherine Puttroff for assisting with data acquisition speeds. We thank Associate Editor Pablo Heresi for his assistance with this manuscript. The manuscript greatly benefited from thoughtful reviews from two reviewers. We also thank Christie Rowe for her organizational help. This research was supported by the U.S. Department of Energy, Office of Science, Office of Basic Energy Sciences, Geosciences program under Award Number DE-SC0016527170455-00001.

Data and Code Availability

Seismic catalogs were obtained from the USGS ComCat interface (last accessed June 2023; Kilb and Vernon, 2025a). Focal mechanisms for the two events and the additional four small magnitude events were obtained from the Southern California Earthquake Data Center (SCEDC, 2013, https://scedc.caltech.edu/eq-catalogs/focal-mechanisms.html, last accessed March 2026).

Waveform data and seismic station information were obtained from IRIS via the irisFetch.m MATLAB interface (http://www.iris.edu/dms/nodes/dmc/software/downloads/irisFetch.m), last accessed June 2024. The MATLAB code used to process these data (*data_prep_final.m*) is archived on Zenodo (Kilb and Vernon, 2025b). The table of outliers (*Paper_outliers.csv*) (Kilb and Vernon, 2025c) and the table of events that produced the largest ground motions (*large_amps_final.csv*) are also available on Zenodo (Kilb and Vernon, 2025d).

Competing interests

The authors have no competing interests.

References

Abrahamson, N. A., Silva, W. J., and Kamai, R. Summary of the ASK14 Ground Motion Relation for Active Crustal Regions. *Earthquake Spectra*, 30(3):1025–1055, Aug. 2014. doi: 10.1193/070913eqs198m.

Aki, K. and Richards, P. *Quantitative Seismology*. University Science Books, Sausalito, CA, 2nd edition, 2002.

Allen, R. M. and Stogaitis, M. Global growth of earthquake early warning. *Science*, 375(6582):717–718, Feb. 2022. doi: 10.1126/science.abl5435.

Allen, T. I. and Wald, D. J. Topographic Slope as a Proxy for Seismic Site-Conditions (VS30) and Amplification Around the Globe. Open-file report, US Geological Survey, 2007. doi: 10.3133/ofr20071357.

Anderson, J. G. and Hough, S. E. A model for the shape of the fourier amplitude spectrum of acceleration at high frequencies. *Bulletin of the Seismological Society of America*, 74(5): 1969–1993, Oct. 1984. doi: 10.1785/bssa0740051969.

Anthony, R. E., Ringler, A. T., Wilson, D. C., Zebulon Maharrey, J., Gyure, G., Pepiot, A., Sandoval, L. D., Sandoval, S., Telesha, T., Vallo, G., and Voss, N. Installation and Performance of the Albuquerque Seismological Laboratory Small-Aperture Posthole Array. *Seismological Research Letters*, 91(4), 2020. doi: 10.1785/0220200080.

Arrowsmith, S. J., Trugman, D. T., MacCarthy, J., Bergen, K. J., Lumley, D., and Magnani, M. B. Big Data Seismology. *Reviews of Geophysics*, 60(2), May 2022. doi: 10.1029/2021rg000769.

Ben-Zion, Y. and Aki, K. Seismic radiation from an SH line source in a laterally heterogeneous planar fault zone. *Bulletin of the Seismological Society of America*, 80(4):971–994, Aug. 1990. doi: 10.1785/bssa0800040971.

Ben-Zion, Y., Vernon, F. L., Ozakin, Y., Zigone, D., Ross, Z. E., Meng, H., White, M., Reyes, J., Hollis, D., and Barklage, M. Basic data features and results from a spatially dense seismic array on the San Jacinto fault zone. *Geophysical Journal International*, 202 (1):370–380, May 2015. doi: 10.1093/gji/ggv142.

Boore, D. M. The Richter scale: its development and use for determining earthquake source parameters. *Tectonophysics*, 166 (1-3), 1989. doi: 10.1016/0040-1951(89)90200-x.

Borcherdt, R. D. Estimates of site-dependent response spectra for design (methodology and justification). *Earthquake Spectra*, 10 (4):617–653, Nov. 1994. doi: 10.1193/1.1585791.

Brune, J. Tectonic stress and the spectra of seismic shear waves from earthquakes. *Journal of Geophysical Research*, 75(26), 1970. doi: 10.1029/jb075i026p04997.

Chang, H., Abercrombie, R. E., and Nakata, N. Importance of Considering Near-Surface Attenuation in Earthquake Source Parameter Estimation: Insights from Kappa at a Dense Array in Oklahoma. *Bulletin of the Seismological Society of America*, 115(3): 947–964, Jan. 2025. doi: 10.1785/0120240137.

Chatterjee, A., Trugman, D. T., Hirth, G., Lee, J., and Tsai, V. C. High-Frequency Ground Motions of Earthquakes Correlate With Fault Network Complexity. *Geophysical Research Letters*, 51(12), 2024. doi: 10.1029/2024gl109418.

Cochran, E. S., Saunders, J. K., Minson, S. E., Bunn, J., Baltay, A., Kilb, D., O'Rourke, C., Hoshiba, M., and Kodera, Y. Alert Optimization of the PLUM Earthquake Early Warning Algorithm for the Western United States. *Bulletin of the Seismological Society of America*, 112(2):803–819, Jan. 2022. doi: 10.1785/0120210259.

Cormier, V. F. and Spudich, P. Amplification of ground motion and waveform complexity in fault zones: examples from the San Andreas and Calaveras Faults. *Geophysical Journal International*, 79(1):135–152, Oct. 1984. doi: 10.1111/j.1365-246x.1984.tb02846.x.

Douglas, J. and Edwards, B. Recent and future developments in earthquake ground motion estimation. *Earth-Science Reviews*, 160, 2016. doi: 10.1016/j.earscirev.2016.07.005.

Given, D. D., Cochran, E. S., Heaton, T., Hauksson, E., Allen, R., Hellweg, P., Vidale, J., and Bodin, P. Technical implementation plan for the ShakeAlert production system: an Earthquake Early Warning system for the West Coast of the United States. Open-file report, US Geological Survey, 2014. doi: 10.3133/ofr20141097.

Graves, R. W., Aagaard, B. T., Hudnut, K. W., Star, L. M., Stewart, J. P., and Jordan, T. H. Broadband simulations for Mw 7.8 southern San Andreas earthquakes: Ground motion sensitivity to rupture speed. *Geophysical Research Letters*, 35(22), Nov. 2008. doi: 10.1029/2008gl035750.

Hanks, T. C. and Boore, D. M. Moment-magnitude relations in theory and practice. *Journal of Geophysical Research: Solid Earth*, 89(B7), 1984. doi: 10.1029/jb089ib07p06229.

Hanks, T. C. and Kanamori, H. A moment magnitude scale. *Journal of Geophysical Research: Solid Earth*, 84(B5), 1979. doi: 10.1029/jb084ib05p02348.

Heath, D. C., Wald, D. J., Worden, C. B., Thompson, E. M., and Smoczyk, G. M. A global hybrid VS 30 map with a topographic slope–based default and regional map insets. *Earthquake Spectra*, 36(3):1570–1584, Aug. 2020. doi: 10.1177/8755293020911137.

Hirakawa, E., Parker, G. A., Baltay, A., and Hanks, T. Rupture Directivity of the 25 October 2022 Mw 5.1 Alum Rock Earthquake. *The Seismic Record*, 3(2):144–155, Apr. 2023. doi: 10.1785/0320230013.

Huddleston, G. J., Schleicher, L. S., Knudsen, K. L., Gee, L. S., and Steidl, J. H. Compilation of Geologic and Seismic Velocity Characteristics at Advanced National Seismic System Strong Motion Accelerometer Sites, 2021. doi: 10.5066/P9YKIUW2.

Iervolino, I., J., and Pike, R. Ground-Motion Observations and Probabilistic Seismic Hazard: Frequently Asked Questions. *Seismological Research Letters*, 93(4), 2022. doi: 10.1785/0220210321.

IRIS Transportable Array. USArray Transportable Array, 2003. doi: 10.7914/SN/TA.

Iwahashi, J. and Pike, R. Automated classifications of topography from DEMs by an unsupervised nested-means algorithm and a three-part geometric signature. *Geomorphology*, 86(3-4), 2007. doi: 10.1016/j.geomorph.2006.09.012.

Johnson, C. W., Meng, H., Vernon, F., and Ben-Zion, Y. Characteristics of Ground Motion Generated by Wind Interaction With Trees, Structures, and Other Surface Obstacles. *Journal of Geophysical Research: Solid Earth*, 124(8):8519–8539, Aug. 2019. doi: 10.1029/2018jb017151.

Johnson, C. W., Kilb, D., Baltay, A., and Vernon, F. Peak Ground Velocity Spatial Variability Revealed by Dense Seismic Array in Southern California. *Journal of Geophysical Research: Solid Earth*, 125(6), 2020. doi: 10.1029/2019jb019157.

Kilb, D. and Vernon, F. Southern California earthquake catalog (ComCat, magnitude 2.5+, 2010-09 to 2023-06), 2025a. doi: 10.5281/ZENODO.17931800.

Kilb, D. and Vernon, F. MATLAB code to compute peak ground motions (PGV and PGA) from seismic waveform data and compile associated metadata, 2025b. doi: 10.5281/ZENODO.14750838.

Kilb, D. and Vernon, F. Peak ground motions generated by earthquakes (magnitude 2.5+, September 2010 - June 2023, southern California) that are larger or smaller than theoretically expected, 2025c. doi: 10.5281/ZENODO.14735940.

Kilb, D. and Vernon, F. List of southern California earthquakes (September 2010 - June 2023) that generated the largest ground motions at stations within seven small aperture arrays, 2025d. doi: 10.5281/ZENODO.14750802.

Kilb, D., Gomberg, J., and Bodin, P. Aftershock triggering by complete Coulomb stress changes. *Journal of Geophysical Research: Solid Earth*, 107(B4), Apr. 2002. doi: 10.1029/2001jb000202.

Kilb, D., Martynov, V. G., and Vernon, F. L. Aftershock Detection Thresholds as a Function of Time: Results from the ANZA Seismic Network following the 31 October 2001 ML 5.1 Anza, California, Earthquake. *Bulletin of the Seismological Society of America*, 97(3), 2007. doi: 10.1785/0120060116.

Kilb, D., Biasi, G., Anderson, J., Brune, J., Peng, Z., and Vernon, F. L. A comparison of spectral parameter kappa from small and moderate earthquakes using southern California ANZA seismic network data. *Bulletin of the Seismological Society of America*, 102 (1), 2012. doi: 10.1785/0120100309.

Kilb, D., Fan, W., and Laske, G. Semantics at the Salton Sea: When does a swarm become a sequence? *Temblor*, 2021. doi: 10.32858/temblor.181.

Kohler, M. D., Smith, D. E., Andrews, J., Chung, A. I., Hartog, R., Henson, I., Given, D. D., de Groot, R., and Guiwits, S. Earthquake Early Warning ShakeAlert 2.0: Public Rollout. *Seismological Research Letters*, 91(3):1763–1775, Apr. 2020. doi: 10.1785/0220190245.

Kurzon, I., Vernon, F. L., Ben-Zion, Y., and Atkinson, G. Ground Motion Prediction Equations in the San Jacinto Fault Zone: Significant Effects of Rupture Directivity and Fault Zone Amplification. *Pure and Applied Geophysics*, 171(11):3045–3081, May 2014. doi: 10.1007/s00024-014-0855-2.

Lentas, K., Evangelidis, C., and Karastathis, V. Designing small-aperture seismic arrays to enhance earthquake monitoring on ocean islands: Application to Antikythera island, Greece. *Seismica*, 5(1), Feb. 2026. doi: 10.26443/seismica.v5i1.1720.

Li, M., Rathje, E. M., Cox, B. R., and Yust, M. A Texas-specific VS30 map incorporating geology and VS30 observations. *Earthquake Spectra*, 38(1):521–542, Feb. 2022. doi: 10.1177/87552930211033622.

Li, Y.-G., Leary, P., Aki, K., and Malin, P. Seismic Trapped Modes in the Oroville and San Andreas Fault Zones. *Science*, 249(4970): 763–766, Aug. 1990. doi: 10.1126/science.249.4970.763.

Li, Z., Peng, Z., Hollis, D., Zhu, L., and McClellan, J. High-resolution seismic event detection using local similarity for Large-N arrays. *Scientific Reports*, 8(1), Jan. 2018. doi: 10.1038/s41598-018-19728-w.

Lux, A. I., Smith, D., Böse, M., McGuire, J. J., Saunders, J. K., Huynh, M., Stubailo, I., Andrews, J., Lotto, G., Crowell, B., Crane, S., Allen, R. M., Given, D., Hartog, R., Heaton, T., Husker, A., Marty, J., O'Driscoll, L., Tobin, H., McBride, S. K., and Toomey, D. Status and Performance of the ShakeAlert Earthquake Early Warning System: 2019–2023. *Bulletin of the Seismological Society of America*, 114(6):3041–3062, Aug. 2024. doi: 10.1785/0120230259.

Meng, H. and Ben-Zion, Y. Detection of small earthquakes with dense array data: example from the San Jacinto fault zone, southern California. *Geophysical Journal International*, 212(1), 2017. doi: 10.1093/gji/ggx404.

Meng, H., Ben-Zion, Y., and Johnson, C. W. Analysis of Seismic Signals Generated by Vehicle Traffic with Application to Derivation of Subsurface Q-Values. *Seismological Research Letters*, 92(4): 2354–2363, Feb. 2021. doi: 10.1785/0220200457.

Minson, S. E., Baltay, A. S., Cochran, E. S., McBride, S. K., and Milner, K. R. Shaking is Almost Always a Surprise: The Earthquakes That Produce Significant Ground Motion. *Seismological Research Letters*, 92(1):460–468, Nov. 2020. doi: 10.1785/0220200165.

Mordret, A., Roux, P., Boué, P., and Ben-Zion, Y. Shallow three-dimensional structure of the San Jacinto fault zone revealed from ambient noise imaging with a dense seismic array. *Geophysical Journal International*, 216(2):896–905, Nov. 2018. doi: 10.1093/gji/ggy464.

Nye, T., Sahakian, V. J., King, E., Baltay, A., and Klimasewski, A. Estimates of κ0 and Effects on Ground Motions in the San Francisco Bay Area. *Bulletin of the Seismological Society of America*, 113 (2):823–842, Dec. 2022. doi: 10.1785/0120220046.

Olsen, K. B. Site Amplification in the Los Angeles Basin from Three-Dimensional Modeling of Ground Motion. *Bulletin of the Seismological Society of America*, 90(6B):S77–S94, Dec. 2000. doi: 10.1785/0120000506.

Parker, G. A., Harmon, J. A., Stewart, J. P., Hashash, Y. M. A., Kottke, A. R., Rathje, E. M., Silva, W. J., and Campbell, K. W. Proxy-based VS 30 estimation in central and eastern North America. *Bulletin of the Seismological Society of America*, 107(1):117–131, Jan. 2017. doi: 10.1785/0120160101.

Parker, G. A., Baltay, A. S., Rekoske, J., and Thompson, E. M. Repeatable Source, Path, and Site Effects from the 2019 M 7.1 Ridgecrest Earthquake Sequence. *Bulletin of the Seismological Society of America*, 110(4), 2020. doi: 10.1785/0120200008.

Petersen, M. D., Shumway, A. M., Powers, P. M., Field, E. H., Moschetti, M. P., Jaiswal, K. S., Milner, K. R., Rezaeian, S., Frankel, A. D., Llenos, A. L., Michael, A. J., Altekruse, J. M., Ahdi, S. K., Withers, K. B., Mueller, C. S., Zeng, Y., Chase, R. E., Salditch, L. M., Luco, N., Rukstales, K. S., Herrick, J. A., Girot, D. L., Aagaard, B. T., Bender, A. M., Blanpied, M. L., Briggs, R. W., Boyd, O. S., Clayton, B. S., DuRoss, C. B., Evans, E. L., Haeussler, P. J., Hatem, A. E., Haynie, K. L., Hearn, E. H., Johnson, K. M., Kortum, Z. A., Kwong, N. S., Makdisi, A. J., Mason, H. B., McNamara, D. E., McPhillips, D. F., Okubo, P. G., Page, M. T., Pollitz, F. F., Rubinstein, J. L., Shaw, B. E., Shen, Z., Shiro, B. R., Smith, J. A., Stephenson, W. J., Thompson, E. M., Thompson Jobe, J. A., Wirth, E. A., and Witter, R. C. The 2023 US 50-State National Seismic Hazard Model: Overview and implications. *Earthquake Spectra*, 40(1):5–88, Feb. 2024. doi: 10.1177/87552930231215428.

Pischiutta, M., Baker, L. M., Fletcher, J. B., Salvini, F., Rovelli, A., and Ben-Zion, Y. Directional amplification across the San Jacinto fault zone, CA. *Geophysical Journal International*, 238(2), 2024. doi: 10.1093/gji/ggae198.

Qin, L., Ben-Zion, Y., Qiu, H., Share, P.-E., Ross, Z. E., and Vernon, F. L. Internal structure of the San Jacinto fault zone in the trifurcation area southeast of Anza, California, from data of dense seismic arrays. *Geophysical Journal International*, 213(1): 98–114, Dec. 2017. doi: 10.1093/gji/ggx540.

Qiu, H., Ben-Zion, Y., Ross, Z., Share, P.-E., and Vernon, F. Internal structure of the San Jacinto fault zone at Jackass Flat from data recorded by a dense linear array. *Geophysical Journal International*, 209(3):1369–1388, Mar. 2017. doi: 10.1093/gji/ggx096.

Qiu, H., Ben-Zion, Y., Catchings, R., Goldman, M. R., Allam, A. A., and Steidl, J. Seismic imaging of the Mw 7.1 Ridgecrest earthquake rupture zone from data recorded by dense linear arrays. *Journal of Geophysical Research: Solid Earth*, 126(7), 2021. doi: 10.1029/2021JB022043.

Rahpeyma, S., Halldorsson, B., Hrafnkelsson, B., Green, R. A., and Jónsson, S. Site effect estimation on two Icelandic strong-motion arrays using a Bayesian hierarchical model for the spatial distribution of earthquake peak ground acceleration. *Soil*

Dynamics and Earthquake Engineering, 120:369–385, May 2019. doi: 10.1016/j.soildyn.2019.02.007.

Rathje, E. M., Abrahamson, N. A., and Bray, J. D. Simplified Frequency Content Estimates of Earthquake Ground Motions. *Journal of Geotechnical and Geoenvironmental Engineering*, 124(2):150–159, Feb. 1998. doi: 10.1061/(asce)1090-0241(1998)124:2(150).

Sahakian, V., Baltay, A., Hanks, T., Buehler, J., Vernon, F., Kilb, D., and Abrahamson, N. Decomposing Leftovers: Event, Path, and Site Residuals for a Small-Magnitude Anza Region GMPE. *Bulletin of the Seismological Society of America*, 108(5A), 2018. doi: 10.1785/0120170376.

SCEDC. Southern California Earthquake Center [dataset], 2013. doi: 10.7909/C3WD3xH1.

Schliwa, N., Gabriel, A., and Ben-Zion, Y. Shallow Fault Zone Structure Affects Rupture Dynamics and Ground Motions of the 2019 Ridgecrest Sequence to Regional Distances. *Journal of Geophysical Research: Solid Earth*, 130(6), 2025. doi: 10.1029/2025jb031194.

Share, P., Vernon, F. L., and Ben-Zion, Y. The Variable Continuous Bimaterial Interface in the San Jacinto Fault Zone Revealed by Dense Seismic Array Analysis of Fault Zone Head Waves. *Journal of Geophysical Research: Solid Earth*, 128(2), Feb. 2023. doi: 10.1029/2022jb025070.

Share, P.-E., Ben-Zion, Y., Ross, Z. E., Qiu, H., and Vernon, F. L. Internal structure of the San Jacinto fault zone at Blackburn Saddle from seismic data of a linear array. *Geophysical Journal International*, 210(2):819–832, May 2017. doi: 10.1093/gji/ggx191.

Share, P.-E., Allam, A. A., Ben-Zion, Y., Lin, F.-C., and Vernon, F. L. Structural Properties of the San Jacinto Fault Zone at Blackburn Saddle from Seismic Data of a Dense Linear Array. *Pure and Applied Geophysics*, 176(3), 2018. doi: 10.1007/s00024-018-1988-5.

Share, P. E., Guo, H., Thurber, C. H., Zhang, H., and Ben-Zion, Y. Seismic imaging of the southern California plate boundary around the south-central Transverse Ranges using double-difference tomography. *Pure and Applied Geophysics*, 176(3), 2019. doi: 10.1007/s00024-018-2042-3.

Share, P.-E., Tábořík, P., Štěpančíková, P., Stemberk, J., Rockwell, T. K., Wade, A., Arrowsmith, J. R., Donnellan, A., Vernon, F. L., and Ben-Zion, Y. Characterizing the uppermost 100 m structure of the San Jacinto fault zone southeast of Anza, California, through joint analysis of geological, topographic, seismic and resistivity data. *Geophysical Journal International*, 222(2): 781–794, May 2020. doi: 10.1093/gji/ggaa204.

Steidl, J. H., Tumarkin, A. G., and Archuleta, R. J. What is a reference site? *Bulletin of the Seismological Society of America*, 86(6): 1733–1748, Dec. 1996. doi: 10.1785/bssa0860061733.

Tamhidi, A., Kuehn, N. M., and Bozorgnia, Y. Uncertainty quantification of ground motion time series generated at uninstrumented sites. *Earthquake Spectra*, 39(1):551–576, Feb. 2023. doi: 10.1177/87552930221135286.

Thompson, E. M., Wald, D. J., and Worden, C. B. A VS30 Map for California with Geologic and Topographic Constraints. *Bulletin of the Seismological Society of America*, 104(5), 2014. doi: 10.1785/0120130312.

Trifunac, M. D. Site conditions and earthquake ground motion – A review. *Soil Dynamics and Earthquake Engineering*, 90:88–100, Nov. 2016. doi: 10.1016/j.soildyn.2016.08.003.

U.S. Geological Survey. Quaternary fault and fold database for the United States [dataset], 2004. doi: 10.3133/fs20043033.

U.S. Geological Survey. Advanced National Seismic System (ANSS) Comprehensive Catalog [dataset], 2017. doi: 10.5066/F7MS3QZH.

Vernon, F. L., Fletcher, J., Carroll, L., Chave, A., and Sembera, E. Coherence of seismic body waves from local events as measured by a small-aperture array. *Journal of Geophysical Research: Solid Earth*, 96(B7), 1991. doi: 10.1029/91jb00193.

Vidale, J. and Helmberger, D. Elastic finite-difference modeling of the 1971 San Fernando, California, earthquake. *Bull. Seism. Soc. Am*, page 78122–141, 1988. doi: 10.1785/BSSA0780010122.

Wald, D. J. and Allen, T. I. Topographic Slope as a Proxy for Seismic Site Conditions and Amplification. *Bulletin of the Seismological Society of America*, 97(5):1379–1395, Oct. 2007. doi: 10.1785/0120060267.

Wald, D. J., Quitoriano, V., Heaton, T. H., and Kanamori, H. Relationships between Peak Ground Acceleration, Peak Ground Velocity, and Modified Mercalli Intensity in California. *Earthquake Spectra*, 15(3):557–564, Aug. 1999. doi: 10.1193/1.1586058.

Wang, Y., Allam, A., and Lin, F. Imaging the Fault Damage Zone of the San Jacinto Fault Near Anza With Ambient Noise Tomography Using a Dense Nodal Array. *Geophysical Research Letters*, 46 (22):12938–12948, Nov. 2019. doi: 10.1029/2019gl084835.

Wills, C. J., Gutierrez, C. I., Perez, F. G., and Branum, D. M. A next generation VS30 map for California based on geology and topography. *Bulletin of the Seismological Society of America*, 105 (6):3083–3091, Nov. 2015. doi: 10.1785/0120150105.

Yang, H. and Zhu, L. Shallow low-velocity zone of the San Jacinto fault from local earthquake waveform modelling. *Geophysical Journal International*, 183(1):421–432, Aug. 2010. doi: 10.1111/j.1365-246x.2010.04744.x.

Yang, H., Li, Z., Peng, Z., Ben-Zion, Y., and Vernon, F. Low-velocity zones along the San Jacinto Fault, Southern California, from body waves recorded in dense linear arrays. *Journal of Geophysical Research: Solid Earth*, 119(12):8976–8990, Dec. 2014. doi: 10.1002/2014jb011548.

Yeh, T.-Y. and Olsen, K. B. Fault Damage Zone Effects on Ground Motions during the 2019 Mw 7.1 Ridgecrest, California, Earthquake. *Bulletin of the Seismological Society of America*, 113(4): 1724–1738, Apr. 2023. doi: 10.1785/0120220249.

Yong, A. Comparison of Measured and Proxy-Based VS30 Values in California. *Earthquake Spectra*, 32(1):171–192, Feb. 2016. doi: 10.1193/013114eqs025m.

Yong, A., Hough, S. E., Iwahashi, J., and Braverman, A. A Terrain-Based Site-Conditions Map of California with Implications for the Contiguous United States. *Bulletin of the Seismological Society of America*, 102(1):114–128, Feb. 2012. doi: 10.1785/0120100262.

Zhang, H., Melgar, D., Sahakian, V., Searcy, J., and Lin, J.-T. Learning source, path and site effects: CNN-based on-site intensity prediction for earthquake early warning. *Geophysical Journal International*, 231(3):2186–2204, Aug. 2022. doi: 10.1093/gji/ggac325.

Zigone, D., Ben-Zion, Y., Lehujeur, M., Campillo, M., Hillers, G., and Vernon, F. L. Imaging subsurface structures in the San Jacinto fault zone with high-frequency noise recorded by dense linear arrays. *Geophysical Journal International*, 217(2):879–893, Feb. 2019. doi: 10.1093/gji/ggz069.